Reciprocal discoidin domain receptor signaling strengthens integrin adhesion to connect adjacent tissues

[#]Kieop Park[1], [#]Ranjay Jayadev[1], [#]Sara G. Payne[1,2], Isabel W. Kenny-Ganzert[1], Qiuyi Chi[1], Daniel S. Costa[1], William Ramos-Lewis[1], Siddharthan Balachandar Thendral[1], and [*]David R. Sherwood[1]

[1] Department of Biology, Duke University, Box 90338, Durham, NC 27708, USA

[2] Department of Cell Biology, Duke University Medical Center, Durham, NC 27708, USA

[#]Shared first author
[*]Correspondence: david.sherwood@duke.edu

Running title: DDR-2 signaling connects tissues

Key words: Discoidin domain receptor, type IV collagen, integrin, endocytosis, Ras, basement membrane, tissue connection

Abstract

Separate tissues connect through adjoining basement membranes to carry out molecular barrier, exchange, and organ support functions. Cell adhesion at these connections must be robust and balanced to withstand independent tissue movement. Yet, how cells achieve synchronized adhesion to connect tissues is unknown. Here, we have investigated this question using the *C. elegans* utse-seam tissue connection that supports the uterus during egg-laying. Through genetics, quantitative fluorescence, and cell specific molecular disruption, we show that type IV collagen, which fastens the linkage, also activates the collagen receptor discoidin domain receptor 2 (DDR-2) in both the utse and seam. RNAi depletion, genome editing, and photobleaching experiments revealed that DDR-2 signals through LET-60/Ras to coordinately strengthen an integrin adhesion in the utse and seam that stabilizes their connection. These results uncover a synchronizing mechanism for robust adhesion during tissue connection, where collagen both affixes the linkage and signals to both tissues to bolster their adhesion.

52 **Introduction**

53 Basement membrane (BM) is a planar, cell-associated extracellular matrix (ECM) that underlies
54 or surrounds most tissues. BM provides tissues with structural support, barrier functions, and
55 signaling platforms (Morrissey and Sherwood 2015, Jayadev and Sherwood 2017, Pozzi,
56 Yurchenco et al. 2017). The two core BM matrix components are the heterotrimeric proteins
57 laminin and type IV collagen. Laminin is comprised of an α, β, and γ subunit. Once secreted,
58 laminin associates with cell surface receptors and self-assembles into a sheet-like network.
59 Type IV collagen is a large protein comprised of two α1-like and one α2-like chains, and these
60 heterotrimers cross-link to form a grid, which is thought to be connected to the laminin network
61 through bridging molecules (Hohenester and Yurchenco 2013). Type IV collagen provides BM
62 with tensile strength, which allows BM to structurally support tissues and resist mechanical
63 forces (Fidler, Boudko et al. 2018). Type IV collagen is a ligand for several vertebrate integrin
64 receptors and the collagen-specific receptor tyrosine kinase discoidin domain receptor 1 (DDR1)
65 (Khoshnoodi, Pedchenko et al. 2008, Brown, Cummings et al. 2017). Integrin and DDR1
66 interactions with type IV collagen mediate a wide variety cell-matrix functions, including cell
67 migration and cell adhesion (Khoshnoodi, Pedchenko et al. 2008, Castro-Sanchez, Soto-
68 Guzman et al. 2010, Borza and Pozzi 2014, Xiao, Jiang et al. 2015). DDR receptors and integrin
69 also functionally interact within cells (Leitinger 2014); however, the roles of these interactions in
70 native tissue settings remains poorly defined.

71

72 At tissue interfaces juxtaposed BMs usually slide along each other and maintain distinct tissue
73 boundaries (Sherwood and Sternberg 2003, Brown 2011). At specific sites, however, the BMs of
74 neighboring tissues link to stabilize tissue interactions and build complex organs (Keeley and
75 Sherwood 2019). Examples include the kidney, where podocytes and endothelial BMs connect
76 to form the glomerular BM blood filtration unit (Abrahamson 1985); the brain, where the
77 astrocyte end feet and endothelial BMs join to build the blood-brain barrier (Sixt, Engelhardt et

al. 2001); and the somite, where somite and epidermal BMs link to maintain somite-epidermal association during development (Feitosa, Zhang et al. 2012). Approximately 20 different BM-BM linkages between neighboring tissues have been documented (Gao, Mruk et al. 2017, Keeley and Sherwood 2019, Welcker, Stein et al. 2021). Disruption of these BM-BM tissue connections appear to underlie human diseases, such as in Alport's syndrome, where defects in kidney and hearing are associated with tissue linkage disruption (Merchant, Burgess et al. 2004, Naylor, Morais et al. 2021). Despite the prevalence and importance of BM-BM tissue connections, the challenge of studying tissue interactions *in vivo* has hampered our understanding of the mechanisms establishing and maintaining these linkages.

The simple tissues, visual transparency, and experimental tractability of *C. elegans* offers a powerful model to study BM-BM tissue interactions. Further, most *C. elegans* BM components and receptors are endogenously tagged with genetically encoded fluorophores to visualize localization, levels, and dynamics (Keeley, Hastie et al. 2020, Jayadev, Morais et al. 2022). A BM-BM tissue connection between the large, multinucleated uterine utse cell and epidermal seam cells stabilizes the uterus during egg laying. The utse-seam connection is formed by BMs of the utse and the seam cells, each ~50 nm thick, which are bridged by an ~100 nm connecting matrix (Vogel and Hedgecock 2001, Morrissey, Keeley et al. 2014, Gianakas, Keeley et al. 2023). Disruption of the utse-seam BM-BM tissue linkage results in prolapse of the uterus (**Rup**tured phenotype) out of the animal after the onset of egg-laying. Formation of the utse-seam attachment is initiated by the deposition of the matrix proteins fibulin and hemicentin during the last larval stage of development. Hemicentin promotes the recruitment of type IV collagen, which accumulates at high levels at the BM-BM tissue connection and strengthens the adhesion, allowing it to resist the strong mechanical forces of egg-laying. The utse-seam connection is robust, with each component of the tissue-spanning matrix contributing to the BM-BM connection (Gianakas, Keeley et al. 2023). This likely accounts for the ability of the utse-

seam connection to initially resist mechanical forces after loss of any of these components, delaying the uterine prolapse phenotype until sometime after the initiation of egg-laying. The integrin, αINA-1, one of two *C. elegans* alpha integrins, is also expressed in the utse and is required to prevent uterine-prolapse during egg-laying. However, its regulation and function at the utse-seam connection is unclear (Morrissey, Keeley et al. 2014, Gianakas, Keeley et al. 2023). Mechanisms that link juxtaposed BMs appear to be shared, as hemicentin-1 promotes BM-BM tissue connection in the zebrafish fin fold, hemicentin-2 and fibulin-1 mediate zebrafish somite-epidermis BM-BM association, and hemicentin-1 stabilizes BM-BM linkage at myotendinous junctions in mice (Carney, Feitosa et al. 2010, Feitosa, Zhang et al. 2012, Welcker, Stein et al. 2021). In addition, type IV collagen bridges the podocyte BM and endothelial BM to form the glomerular BM in mice and humans (Suleiman, Zhang et al. 2013, Naylor, Morais et al. 2021). While significant insights are being gained on matrix composition at BM-BM tissue connections, it remains unknown how tissues coordinate and strengthen their adhesive activity at linkage sites. Cells at tissue connections must resist the forces of tissue shifting arising from growth, muscle contraction, and blood flow, and it is unclear how tissues synchronize and bolster adhesions at tissue linkage sites.

Here, we discover that the *C. elegans* discoidin domain receptor DDR-2, an ortholog to the two vertebrate collagen binding DDR tyrosine kinase receptors (RTK), coordinates and strengthens an integrin mediated cell adhesion to support the utse-seam BM-BM tissue linkage during its formation. Using genetics, endogenous tagging, and tissue-specific molecular perturbations, we show that DDR-2 is expressed and functions in the utse and seam cells to mediate utse-seam attachment between the mid and late L4 larval stages. We reveal that assembly of type IV collagen linking the juxtaposed BMs triggers the internalization of DDR-2 in both the utse and seam cells into endocytic vesicles, a signaling compartment for DDR/RTK receptors. In the *ddr-2* knockout mutant, gaps in utse-seam attachment occurred at this time. Through tissue-specific

130 perturbation, quantitative fluorescence analysis, and fluorescence recovery after photobleaching
131 (FRAP), we provide evidence that DDR-2 signals through LET-60/Ras to increase the levels
132 and stability of the α-integrin INA-1 at the utse-seam linkage. Together, these results reveal a
133 mechanism for synchronizing a robust adhesion during tissue linkage, where type IV collagen,
134 which bridges and fastens the BM-BM tissue linkage, also serves as a signal to coordinate, and
135 bolster cell-matrix adhesion in cells on both sides of the tissue connection.
136

137 ## Results

138 **The utse and seam cells associate during the early-L4 stage**

139 The utse is an H-shaped syncytial uterine cell that underlies the *C. elegans* uterus and opens
140 along the central crossbar region during egg-laying to allow embryo passage (Ghosh and
141 Sternberg 2014). The utse is flanked laterally on both sides of the animal by a string of
142 epidermal seam cells that run the length of the body. The utse cell and seam cells are each
143 encased in a BM, which become linked by a specialized matrix whose known functional
144 components include hemicentin, fibulin, and type IV collagen (***Figure 1A***) (Gianakas, Keeley et
145 al. 2023). The BM-BM tissue connection supports the uterus during egg-laying and disruption of
146 the linkage results in uterine prolapse (***Figure 1B and C***) (Vogel and Hedgecock 2001). The
147 utse and seam cells are in contact by the mid L4 larval stage (Gianakas, Keeley et al. 2023), but
148 when the initial contact is established is not known.
149

150 The utse is formed from the fusion of one specialized uterine cell, the anchor cell, with eight
151 adjacent uterine pi cell progeny, forming the syncytial nine-nuclei utse during the early L4 stage
152 (Newman, White et al. 1996, Ghosh and Sternberg 2014). To determine when the utse first
153 contacts the seam cells, we used an anchor cell-specific mCherry fluorophore marker (*cdh-*
154 *3p::mCherry::PLC*δ^{PH}; ***Figure 1D***, arrow) (Hagedorn, Yashiro et al. 2009) that diffuses into the

155 uterine pi cell progeny during fusion and simultaneously viewed a GFP seam cell marker
156 (*scmp::GFP::CAAX*) (Chapman, Li et al. 2008). We found that the utse contacts the seam cells
157 during the early L4 stage as the utse syncytium forms (***Figure 1D***, arrowheads; n=5/5 cases
158 observed). Shortly after utse-seam contact, the BM-BM linkage is initiated at the mid L4 stage
159 by the assembly of low levels of hemicentin, which is secreted by the utse and fibulin-1, which
160 hemicentin recruits from the extracellular fluid. Fibulin-1 and hemicentin protect the utse-seam
161 cell connection from mechanical forces arising from body movement and uterine and vulval
162 muscle contractions prior to egg-laying (Gianakas et al. 2023). Hemicentin also promotes
163 recruitment of type IV collagen from the extracellular fluid, which allows the utse-seam BM-BM
164 connection to resist the strong mechanical forces from egg-laying (Gianakas et al. 2023)
165 (***Figure 1D***). Together, these results show that the utse and seam cells are in contact prior to
166 deposition of matrix components that strengthen the utse-seam BM-BM tissue connection.
167
168 **Loss of discoidin domain receptor-2 (DDR-2) causes uterine prolapse**
169 As type IV collagen is critical to the BM-BM connection, we were next interested in
170 understanding how receptors for type IV collagen regulate the utse-seam BM-BM linkage. The
171 two main receptors for type IV collagen are integrin and the discoidin domain receptor (DDR)
172 (Fidler, Boudko et al. 2018). *C. elegans* harbor two integrin heterodimers composed of different
173 α chains with a shared β chain: αINA-1/ βPAT-3 and αPAT-2/ βPAT-3 (Clay and Sherwood
174 2015). The integrin INA-1 is expressed in the utse and its loss leads to uterine prolapse,
175 suggesting a possible role in utse-seam attachment (Morrissey, Keeley et al. 2014, Gianakas,
176 Keeley et al. 2023). Whether DDRs function at the utse-seam connection, however, is unknown.
177
178 *C. elegans* have two DDR genes, *ddr-1* and *ddr-2,* which are paralogs and orthologs to the two
179 mammalian DDRs (Vogel, Abdulhussein et al. 2006). Like mammalian counterparts, the *C.*

180 *elegans* DDRs are comprised of discoidin and discoidin-like domains, followed by a
181 transmembrane domain and a kinase domain (***Figure 2A***). To determine if *C. elegans* DDRs
182 play a role in utse-seam BM-BM linkage, we examined several *ddr-1* and *ddr-2* mutants (***Figure***
183 ***2A***). We first screened for the Rup phenotype caused by uterine prolapse, observing animals
184 every day during the egg-laying period, from its onset (48 h post-L1) to end (120 h) (***Methods***).
185 Animals harboring the *ddr-1(ok874)* deletion allele, which eliminates the intracellular portion of
186 DDR-1, and animals with the *ddr-1(tm382)* allele containing an early stop codon truncating the
187 majority of the predicted protein (Unsoeld, Park et al. 2013), did not show a Rup phenotype
188 (***Figure 2A and B***). In contrast, animals homozygous for the *ddr-2(tm797)* allele, which
189 introduces an early stop codon and is thought to be a null or strong loss-of-function (Unsoeld,
190 Park et al. 2013), exhibited a significant Rup/uterine prolapse defect. Animals carrying the *ddr-*
191 *2(ok574)* allele, which deletes a portion of the intracellular kinase domain (Unsoeld, Park et al.
192 2013), also showed an increased frequency of the Rup phenotype compared to wild-type
193 animals, although this difference was not statistically significant (***Figure 2A and B***). We further
194 generated a full-length *ddr-2* deletion allele, *ddr-2(qy64)*, and confirmed that complete loss of
195 *ddr-2* led to a significant uterine prolapse defect (***Figure 2A and B***). Taken together, these
196 results indicate that DDR-2 protects against uterine prolapse and may play a role in mediating
197 utse-seam BM-BM attachment.

198

199 **DDR-2 maintains utse-seam attachment during formation of the tissue connection**

200 To determine if the Rup phenotype observed in *ddr-2* mutants is a result of perturbations in the
201 utse-seam BM-BM tissue connection, we examined utse-seam association from the late L3
202 through young adult stages in animals harboring the *ddr-2*(*qy64)* deletion allele (***Figure 2C***). We
203 visualized utse-seam association using the utse and seam cell membrane markers *cdh-*

204 *3p::mCherry::PLCδ^{PH}* and *scmp::GFP::CAAX,* respectively. Animals homozygous for *ddr-*
205 *2(qy64)* had normal utse-seam cell association at the early L4 stage; however, beginning at the
206 mid L4 stage, gaps in the utse-seam attachment were detected in about 30% of animals. The
207 frequency of gaps increased to ~40% of animals by the mid-to-late L4 and persisted at a similar
208 penetrance to young adulthood (***Figure 2C and D***). In addition, membrane projections
209 emanating from the central body of the utse were detected in *ddr-2(qy64)* animals. These
210 projections were first observed at the mid L4 stage and persisted to young adulthood (***Figure***
211 ***2C***). These observations suggest that DDR-2 functions around the mid L4 to late L4 stages to
212 promote utse-seam attachment, and that DDR-2 may also regulate utse morphology. Next, we
213 wanted to determine if the utse-seam detachment observed in *ddr-2(qy64)* mutants led to
214 uterine prolapse. Wild-type and *ddr-2(qy64)* animals were mounted and imaged at the L4 larval
215 stage for utse-seam attachment defects, recovered, and tracked to the 72-hour adult stage,
216 where they were examined for the Rup phenotype. All wild-type L4 larvae had intact utse-seam
217 attachment and did not rupture by 72-hour adulthood (n=8/8 animals). However, among nine
218 *ddr-2(qy64)* mutant animals examined, four exhibited utse-seam detachments at the L4 stage,
219 all of which underwent uterine prolapse (Rup) by adulthood. The remaining five *ddr-2* mutant
220 animals, which had an intact utse-seam linkage, did not display the Rup phenotype. Taken
221 together, these results suggest that DDR-2 promotes utse-seam attachment during early stages
222 of tissue linkage.

223

224 **DDR-2 is found within endocytic vesicles in the utse and seam cells during initial stages**
225 **of tissue attachment**

226 As utse-seam detachment in *ddr-2* mutant animals was first observed at the mid L4 larval stage,
227 we next sought to determine if DDR-2 was expressed in the utse, seam, or both cell types at
228 this time. Between the mid L4 and late L4 stage, the utse-seam tissue connection forms into a

229 tongue-and-groove association between the utse (tongue) and seam (groove) (***Figure 2D and***
230 ***Figure 2—video 1***). To resolve whether DDR-2 is localized within the seam, utse, or both
231 (Vogel and Hedgecock 2001), we used either a utse (*cdh-3p::mCherry::PLC*δ^{PH}) or seam cell
232 marker (*scmp::2xmKate2::PLC*δ^{PH}), and imaged endogenously tagged DDR-2 protein (DDR-
233 2::mNG) (Keeley, Hastie et al. 2020) in lateral confocal sections from the L4 to young adult
234 stages (***Figure 3A***). We first examined the seam cells contacting the utse (***Figure 3B***). At the
235 early L4 stage DDR-2::mNG was faintly visible at the surface of the seam cells and found in a
236 few intracellular punctae (***Figure 3B,*** n=10/10 animals). By the mid L4 stage, DDR-2 was
237 predominantly found in punctae in the region of attachment with the utse. Levels of punctae
238 increased until the late L4 stage and then declined sharply by the young adult (***Figure 3B***).
239 Notably, at the late L4, when DDR-2 punctate localization was at its highest, we could not detect
240 any DDR-2 signal at the cell surface (***Figure 3B,*** n = 9/9). We further examined DDR-2::mNG in
241 seam cells that were not contacting the utse and found that DDR-2 levels were uniformly low
242 from the early L4 through the young adult stages (***Figure 3—figure supplement 1A***). We next
243 investigated DDR-2 localization in the utse contacting the seam. Like the seam cells at the
244 tissue connection site, DDR-2 in the utse was punctate and peaked in levels between the mid
245 and late L4 stages and then declined rapidly (***Figure 3C***). We conclude that DDR-2 is present at
246 high levels and localized within punctate structures in the seam and utse cells at the time when
247 utse-seam defects are observed in *ddr-2* mutant animals.
248
249 Receptor tyrosine kinases (RTKs), including DDRs, are activated upon ligand binding and then
250 rapidly internalized into endocytic vesicles: first the early endosome (marked by RAB-5),
251 followed by subsequent sorting for either lysosome-mediated degradation via late endosomes
252 (marked by RAB-7), or recycled back to the cell surface in recycling endosomes (marked by
253 RAB-11) (Goh and Sorkin 2013). In vertebrates, the exposure of cells to collagen results in the

254 internalization of DDR1b into Rab5a positive early endosomes (Mihai, Chotani et al. 2009).
255 Phosphorylation of DDR1 does not occur until the onset of endocytosis and recycling,
256 suggesting that receptor activation occurs in endocytic vesicles (Mihai, Chotani et al. 2009, Fu,
257 Valiathan et al. 2013). As *C. elegans* DDR-2 appeared to be functioning during the mid L4 to
258 late L4 stages, when levels of DDR-2 were highest and present in vesicular structures, we
259 sought to determine whether DDR-2 was internalized within endocytic vesicles. We examined
260 localization of DDR-2::mNG punctae in relation to utse-expressed markers of early endosomes
261 (*cdh-3p::mCherry::rab-5*), late endosomes (*cdh-3p::mCherry::rab-7*), and recycling endosomes
262 (*cdh-3p::mCherry::rab-11*) (Sato, Norris et al. 2014). DDR-2 was co-localized with all three
263 classes of endosomes in the utse, with the highest overlap with RAB-5 early endosomes
264 (***Figure 3—figure supplement 1B***). In addition, we examined an early endosome marker
265 expressed in seam cells (*scmp::mKate2::rab-5*) and observed DDR-2::mNG punctae co-
266 localized with RAB-5 vesicles (***Figure 3—figure supplement 1C***). The presence of DDR-2 in
267 endocytic vesicles within the utse and seam suggested that DDR-2 signaling may be required
268 for utse-seam attachment. Consistent with this, animals harboring the *ddr-2(ok574)* mutant
269 allele, where a portion of the intracellular kinase domain is deleted (***Figure 2A***), exhibited
270 significant utse-seam detachments at the late L4 stage (***Figure 4A***). Taken together, these
271 observations suggest that DDR-2 functions in the utse and seam cells to promote attachment at
272 the tissue linkage site between the mid and late L4 stages, where it may signal within endocytic
273 vesicles.

274

275 **Type IV collagen promotes DDR-2 vesiculation**

276 DDR signaling is triggered by collagen binding, and vertebrate DDRs bind multiple collagens
277 with different binding affinities (Leitinger 2014). Genetic interaction studies in *C. elegans*
278 revealed that transmembrane collagen COL-99, which is most similar to transmembrane

collagen type XIII, XXIII, and XXV in vertebrates (Tu, Huhtala et al. 2015), may act as a ligand for *C. elegans* DDR-1 and DDR-2 during axon guidance and that type IV collagen might act as a ligand for DDR-2 during axon regeneration (Hisamoto, Nagamori et al. 2016, Taylor, Unsoeld et al. 2018). *C. elegans* BMs also harbor type XVIII collagen (CLE-1) (Keeley, Hastie et al. 2020). Thus, we next investigated whether any of these cell and BM-associated collagens could function as a ligand for DDR-2 at the utse-seam BM-BM tissue connection site.

Type IV collagen enriches at the utse-seam BM-BM linkage during its maturation and helps the connected tissues resist the mechanical forces of egg-laying. In contrast, type XVIII collagen is not present enriched at the linkage (Gianakas, Keeley et al. 2023). Whether COL-99 localizes to the utse-seam tissue linkage is unknown. We thus first examined an endogenously tagged COL-99 (mNG::COL-99) (Jayadev, Morais et al. 2022) and compared its localization and levels to type IV collagen (α1-type IV collagen::mNG (EMB-9::mNG)) and type XVIII collagen (CLE-1::mNG) (Keeley, Hastie et al. 2020) at the utse-seam connection in late L4 animals. COL-99 was not detected while EMB-9 was present at nearly 8-fold higher levels than CLE-1, suggesting that type IV collagen might be the ligand for DDR-2 (***Figure 4B***). Furthermore, the enrichment of type IV collagen levels at the utse-seam connection site occurs rapidly from the mid L4 to late L4 stage (Gianakas, Keeley et al. 2023), correlating with the buildup of DDR-2 in endosomes in the utse and seam cells.

As exposure to collagen triggers vesiculation of vertebrate DDR1b into endocytic vesicles, we wanted to determine whether type IV collagen controls vesiculation of DDR-2 at the utse-seam BM-BM connection. RNAi-mediated depletion of type IV collagen from the L1 through the late L4 larval stages resulted in a sharp decrease in vesicular DDR-2::mNG in the utse and seam cells at the linkage site, accompanied by enrichment of DDR-2 at cell surfaces (***Figure 4C;*** ***Figure 4—figure supplement 1A***). In contrast, reduction of COL-99 and type XVIII collagen did

305 not significantly affect DDR-2 vesiculation (***Figure 4C; Figure 4—figure supplement 1B and***
306 ***C***). Depletion of hemicentin, which plays a crucial role in recruiting type IV collagen to the BM-
307 BM linking matrix (Gianakas, Keeley et al. 2023), also resulted in a significant reduction in DDR-
308 2 vesiculation (***Figure 4D; Figure 4—figure supplement 1D***). In addition, we did not detect
309 DDR-2 at the cell surface, suggesting that hemicentin has a role in recruiting DDR-2 to the site
310 of utse-seam attachment. It is possible that collagen could also function in DDR-2 recruitment,
311 but we could not assess this definitively due to the lower knockdown efficiency of *emb-9* RNAi
312 (***Figure 4—figure supplement 1A***). Together, these findings indicate that type IV collagen
313 assembly at the site of utse-seam BM-BM tissue linkage triggers DDR-2 vesiculation and may
314 act as a ligand for DDR-2 activation to promote utse-seam attachment.
315

316 **DDR-2 functions in the utse and the seam to promote utse-seam attachment**

317 Since DDR-2 localizes to both the utse and seam cells, we next investigated where DDR-2
318 functions to promote utse-seam BM-BM attachment. We generated genome edited lines with
319 single-copy insertions of dominant negative (DN) *ddr-2* (Bernadskaya, Brahmbhatt et al. 2019)
320 driven by the *cdh-3* promoter for utse expression or the *scm* promoter for seam expression.
321 Using the utse-specific membrane marker (*nas-22p::2xmKate2::PLC*δ^{PH}) (Park, Pan et al. 2010)
322 and a seam cell membrane marker (*wrt-2p::GFP::PLC*δ^{PH}) (Wildwater, Sander et al. 2011), we
323 found significant utse-seam detachments in both utse-expressed and seam-expressed *DN ddr-2*
324 animals at the late L4 stage (***Figure 4F and G***). Consistent with the timing and vesicular pattern
325 of DDR-2 localization, these results indicate that DDR-2 functions in both the utse and seam
326 between the mid and late L4 stages to promote utse-seam attachment.

327

328 **Loss of DDR-2 increases type IV collagen at the utse-seam BM-BM adhesion site**

329 The matrix components fibulin-1 and hemicentin play early roles in mediating utse-seam
330 attachment and hemicentin promotes recruitment of type IV collagen and further enrichment of
331 fibulin, which strengthens the BM-BM attachment (Gianakas et al. 2023). We thus next asked
332 whether DDR-2 promotes utse-seam linkage by regulating the assembly of fibulin, hemicentin,
333 or type IV collagen at the connecting matrix. Knockdown of *ddr-2* by RNAi did not alter fibulin
334 levels at the late L4 stage (***Figure 5—figure supplement 1A and B***). However, we observed a
335 modest ~20% reduction in hemicentin upon depletion of DDR-2 (***Figure 5—figure supplement***
336 ***1C***). As loss of hemicentin results in utse-seam detachment at the late L4 stage (Gianakas,
337 Keeley et al. 2023), we tested whether a ~20% reduction of hemicentin could cause these
338 defects by initiating RNAi at the early L4, just before the utse forms (***Methods***). We found that
339 utse-seam attachments were intact in all animals at the late L4 stage upon ~20% reduction of
340 hemicentin (n=13/13 and 12/12 control and *him-4* RNAi-treated animals examined respectively;
341 ***Figure 5—figure supplement 1D***), suggesting that the utse-seam detachment defect in *ddr-2*
342 mutant animals is not caused by a modest reduction in hemicentin levels. Interestingly, there
343 was an ~40% increase in type IV collagen levels at the utse-seam connection after RNAi
344 mediated reduction of *ddr-2*, indicating a possible feedback mechanism between DDR-2
345 signaling and collagen assembly (***Figure 5—figure supplement 1E***). In sum, these results
346 indicate that knockdown of *ddr-2* does not decrease the functional levels of key matrix
347 components at the site of utse-seam BM-BM connection, suggesting that DDR-2 does not
348 promote utse-seam attachment by regulating the assembly of the BM-BM linking matrix.

349

350 **DDR-2 promotes integrin function to mediate utse-seam tissue attachment**

351 Studies have indicated that vertebrate DDRs are not strong adhesive receptors (Xu, Bihan et al.
352 2012). Consistent with this, we detected weak DDR-2::mNG fluorescence signals at the cell
353 membranes of the utse and seam. However, we observed strong DDR-2 signals in a vesicular
354 pattern in both tissues. We thus assessed several molecular activities regulated by DDR
355 signaling that might mediate utse-seam attachment. Vertebrate DDRs promote matrix
356 metalloproteinase (MMP) expression and localization (Leitinger 2014). The *C. elegans* genome
357 harbors six MMP genes, named zinc metalloproteinase 1-6 (*zmp-1-6*) (Altincicek, Fischer et al.
358 2010). We examined four available reporters of ZMP localization (ZMP-1::GFP, ZMP-2::GFP,
359 ZMP-3::GFP, and ZMP-4::GFP) (Kelley, Chi et al. 2019). Only ZMP-4 was detected at the utse-
360 seam connection and its localization was not altered by knockdown of *ddr-2* (***Figure 5—figure***
361 ***supplement 1F***). These observations suggest that DDR-2 does not promote utse-seam linkage
362 through regulation of MMPs, although we cannot rule out roles for DDR-2 in promoting the
363 expression or localization of ZMP-5 or ZMP-6.

364

365 DDRs also modulate integrin activity (Leitinger 2014). Cell culture studies have shown that
366 vertebrate DDRs can enhance integrin adhesion and integrin cell surface levels in multiple cell
367 types (Xu, Bihan et al. 2012, Staudinger, Spano et al. 2013, Bayer, Grither et al. 2019). *C.*
368 *elegans* harbor only two integrin receptors, made up of either the α subunit INA-1 or PAT-2
369 dimerized to the sole β subunit PAT-3 (Clay and Sherwood 2015). We previously found that
370 depletion of INA-1 results in a Rup phenotype, but the specific effect on utse-seam BM-BM
371 tissue attachment was not determined (Morrissey, Keeley et al. 2014). Thus, we next asked
372 whether DDR-2 promotes utse-seam attachment through regulation of integrin. First, we
373 analyzed the localization and levels of endogenously tagged INA-1 (αINA-1::mNG) and PAT-2

374 (αPAT-2::2xmNG) (Jayadev, Chi et al. 2019) and found that both integrin α subunits were
375 expressed in the utse and seam tissues and localized to the utse-seam connection region from
376 the mid-L4 stage through young adulthood (***Figure 5A and B; Figure 5—figure supplement***
377 ***2A and B***). Their levels mirrored that of DDR-2, with a peak at the late L4 stage, followed by a
378 drop off in the young adult stage (***Figure 5A and B)***. However, INA-1 levels were at least sixfold
379 greater than PAT-2 (note, each PAT-2 is linked to two mNG molecules, see ***Methods***),
380 suggesting it may have a dominant role in adhesion (***Figure 5A and B***). Loss of *ddr-2* resulted
381 in a significant reduction in levels of both INA-1 and PAT-2 at the utse-seam BM-BM attachment
382 through the L4 larval stage (***Figure 5B***). Taken together these data suggest DDR-2 could
383 function to promote integrin adhesion within each tissue at the utse-seam connection.
384
385 We focused on a possible role for DDR-2 in regulating INA-1 at the utse-seam linkage, as INA-1
386 was present at higher levels compared to PAT-2 (***Figure 5A and B***) and was more enriched at
387 cell surfaces (***Figure 5—figure supplement 2C***). Furthermore, PAT-2 anchors muscle
388 attachments (Moerman and Williams 2006, Gieseler, Qadota et al. 2017) (***Figure 5A***) and its
389 loss leads to paralysis, which eliminates mechanical stress on the tissue connection and
390 prevents defects in the utse-seam attachment (Gianakas, Keeley et al. 2023). To determine if
391 DDR-2 promotes integrin activity, we reduced INA-1 levels at the late L4 stage to 30% by RNAi
392 and assessed whether loss of *ddr-2* enhanced the Rup and utse-seam splitting defects (***Figure***
393 ***5—figure supplement 2D and E)***. Loss of *ddr-2* strongly enhanced the uterine prolapse defect
394 caused by RNAi-mediated knockdown of *ina-1* (***Figure 5C; Figure 5—figure supplement 2D***).
395 In addition, loss of *ddr-2* enhanced the frequency of utse-seam detachments at the late L4 stage
396 upon depletion of INA-1 (***Figure 5D***). We note that utse-seam detachments were not detected
397 upon RNAi against *ina-1* alone, likely due to incomplete knockdown at this timepoint (***Figure***
398 ***5—figure supplement 2D and E***). Together, these observations are consistent with a possible
399 role for DDR-2 in regulating integrin function to promote utse-seam connection.

400

401 To determine where integrin functions to promote utse-seam attachment, we used a previously
402 characterized dominant negative strategy, where expression of the β integrin PAT-3 lacking the
403 extracellular domain (referred to as *DN integrin*; ***Figure 5E***) inhibits endogenous integrin
404 function (Martin-Bermudo and Brown 1999, Lee, Cram et al. 2001, Hagedorn, Yashiro et al.
405 2009). We used the utse-specific *zmp-1*$^{mK50-51}$ promoter (***Figure 5—figure supplement 2F***)
406 (Hagedorn, Yashiro et al. 2009) and the seam-specific *wrt-2* promoter to disrupt integrin activity
407 in the respective tissues through the time of utse-seam tissue linkage (late L3 to young adult
408 stages, ***Figure 1D***). Expression of *DN integrin* in either the utse or the seam cells resulted in
409 utse-seam detachment at the late L4 (***Figure 5F and G***). Taken together, these findings indicate
410 that DDR-2 may promote utse-seam BM-BM adhesion in part by regulating integrin levels and
411 function.

412

413 **DDR-2 promotes vinculin localization and integrin stability at the utse-seam linkage**

414 As DDR-2 promotes integrin localization to the utse-seam BM-BM linkage and integrin activity
415 promotes utse-seam attachment, we further explored how DDR-2 may regulate integrin. Talin
416 and vinculin are core components of the integrin adhesion complex that support integrin
417 activation (Chastney, Conway et al. 2021). We thus examined endogenously tagged talin
418 (GFP::TLN-1) (Walser, Umbricht et al. 2017) and vinculin (DEB-1::mNG) localization and
419 detected both proteins at the utse-seam attachment site. Levels of each protein ramped up to
420 the late L4 and then decreased by the young adult stage, mirroring DDR-2 (***Figure 6A and B***).
421 However, loss of *ddr-2* only decreased DEB-1 levels (***Figure 6B***). Confirming a role in utse-
422 seam connection, depletion of DEB-1 by RNAi resulted in utse-seam detachment at the late L4
423 stage (***Figure 6C; Figure 6—figure supplement 1***). These data show DDR-2 also regulates
424 vinculin levels at the utse-seam linkage and that vinculin is required for utse-seam attachment.

425

426 Integrin adhesions form stable complexes that anchor cells to ECM (Chastney, Conway et al.
427 2021). To determine whether DDR-2 regulates integrin complex stability at the site of utse-seam
428 BM-BM tissue connection, we analyzed the dynamics of INA-1 by performing Fluorescence
429 Recovery After Photobleaching (FRAP) experiments. We focused on INA-1::mNG at the late L4
430 stage when DDR-2 peaks in levels. Strikingly, loss of *ddr-2* nearly doubled the rate of recovery
431 of INA-1::mNG fluorescence signal in the bleached region 10 minutes post-bleaching as
432 compared to wild-type animals (***Figure 6D***). These observations indicate that DDR-2 stabilizes
433 the INA-1 integrin adhesion complex at the utse-seam adhesion site.

434

435 **Ras acts in the DDR-2 pathway and promotes integrin adhesion at the utse-seam linkage**
436 Vertebrate DDR2 activates multiple signaling networks, including the PI3K/Akt and Ras/Raf/Erk
437 cascades (Payne and Huang 2014, Chen, Kong et al. 2021). Notably, Ras regulates integrin
438 activity in several mammalian cell types (Zhang, Vuori et al. 1996, Conklin, Ada-Nguema et al.
439 2010, Sandri, Caccavari et al. 2012, Lilja, Zacharchenko et al. 2017). We thus hypothesized that
440 DDR-2 could promote integrin stabilization through Ras signaling. We first strongly depleted
441 LET-60 (see ***Methods***) the *C. elegans* Ras ortholog, and observed penetrant utse-seam
442 attachment defects, which were not worsened in *ddr-2* null mutant animals (***Figure 7A***). This
443 suggests that DDR-2 and LET-60/Ras function in the same pathway to mediate the utse-seam
444 connection. Next, we analyzed INA-1::mNG levels and stability after LET-60 reduction. RNAi
445 against *let-60* resulted in significantly lower INA-1 levels at the utse-seam BM-BM connection
446 site (***Figure 7B***, pre-bleach panels and ***Figure 7—figure supplement 1***). Further, like loss of
447 *ddr-2*, FRAP analysis indicated that depletion of LET-60/Ras reduced the stability of INA-1 at
448 the utse-seam linkage site (*i.e.,* there was more rapid recovery of INA-1 after photobleaching
449 (***Figure 7B***). We also generated animals harboring a gain-of-function mutation in Ras (LET-
450 60^{G13E}, *let-60(qy203)*) (Singh and Han 1995). Strikingly, utse-seam detachments were observed

451 in *let-60* gain-of-function animals (***Figure 7C***) and FRAP experiments revealed that INA-1 had
452 an approximately two-fold greater stability at the utse-seam BM-BM connection site (***Figure***
453 ***7D***). Collectively, these findings suggest that Ras acts downstream of DDR-2 to set the
454 appropriate levels and stability of INA-1 mediated adhesion during the formation the utse-seam
455 BM-BM tissue connection.
456

457 **Discussion**

458 To form organs such as the brain, kidney, and lung, separate tissues connect through adjoining
459 basement membrane (BM) to mediate complex functions, such as molecular barrier, blood
460 filtration, and gas exchange, respectively (Keeley and Sherwood 2019). These linkages resist
461 the independent movement of each tissue and must be strong and balanced. How cells
462 coordinate and strengthen adhesion at BM-BM linkage sites, however, is unknown. Using the *C.*
463 *elegans* utse-seam BM-BM tissue connection, we show that type IV collagen, which is the
464 molecular glue that fastens the BM-BM linkage, also activates the *C. elegans* collagen receptor
465 DDR-2 in the utse and seam tissues. DDR-2 activity synchronizes and bolsters an integrin
466 mediated adhesion to stabilize the utse-seam BM-BM tissue connection during its formation
467 (***Figure 8***).
468

469 The linkage between the multi-nucleated utse cell and epithelial seam cells allows the utse to
470 maintain the uterus within the animal during powerful egg-laying muscle contractions (Vogel and
471 Hedgecock 2001). We found that contact between the BM encased utse and seam cells occurs
472 at the time the utse cell is formed during the early L4 larval stage. This association happens just
473 prior to assembly of type IV collagen at the BM-BM linkage, a matrix component that allows the
474 linkage to resist the mechanical forces of egg-laying (Gianakas, Keeley et al. 2023). Even
475 before egg-laying, however, the utse-seam linkage resists the forces of body wall and uterine
476 muscle contractions, as defects in matrix assembly linking the BMs results in utse-seam

477 detachment during the mid L4 stage (Gianakas, Keeley et al. 2023). Through analysis of genetic
478 mutations in the *C. elegans* receptor tyrosine kinase (RTK) DDR-2, an ortholog to the two
479 vertebrate DDR receptors (DDR1 & DDR2) (Unsoeld, Park et al. 2013), we discovered that loss
480 of *ddr-2* results in utse-seam detachment beginning at the mid L4 stage. The frequency of
481 detachments in *ddr-2* mutant animals peaked around the late L4 stage and did not increase
482 after this time. This correlated with the levels of DDR-2::mNG at the utse-seam connection,
483 which peaked at the late L4 stage and then sharply declined by adulthood. Together, these
484 findings suggest that DDR-2 promotes utse-seam attachment in the early formation of the tissue
485 connection between the mid and late L4 stage. Analysis of the BM-BM connecting matrix that
486 links the BMs, which is composed of hemicentin, fibulin-1, and type IV collagen, revealed it was
487 still assembled at functional levels. This suggests that the utse and seam detachment did not
488 arise from a reduction in deposition of BM-BM linking matrix, but rather a defect in tissue
489 adhesion to the BM-BM linkage site. Our results also indicated that DDR-2 functions in both the
490 utse and seam to promote adhesion, as tissue specific expression of a dominant negative DDR-
491 2 in either tissue resulted in utse-seam detachment. Loss of DDR1 in mice disrupts the BM-BM
492 connection between the podocytes and endothelial cells in the kidney glomeruli and leads to
493 defects in blood filtration (Gross, Beirowski et al. 2004), suggesting a possible shared function
494 of DDR receptors in mediating proper linkage at sites of tissue connection.
495
496 In vitro studies using DDR-specific collagen binding peptides have revealed that DDRs only
497 modestly contribute directly to cell adhesion (Xu, Bihan et al. 2012). Instead, DDRs are thought
498 to initiate downstream signaling cascades that promote cell adhesion (Borza and Pozzi 2014).
499 Consistent with this notion, we observed that DDR-2::mNG was not detectable at utse and
500 seam cell surfaces when the *ddr-2* mutant attachment defect occurred between the mid to late
501 L4 stages. Instead, DDR-2 was present in early, late, and recycling endosomes of both utse and
502 seam cells. Work in a mouse osteoblast and a human kidney cell line has shown that DDR1

503 shifts from localization at the cell membrane to aggregation and internalization into early
504 endosomes within minutes of exposure to collagen (Mihai, Chotani et al. 2009). Examination of
505 the timing of DDR activation has suggested that full tyrosine receptor activation occurs within
506 the endocytic vesicles (Mihai, Chotani et al. 2009, Fu, Valiathan et al. 2013)—a signaling hub of
507 other RTKs (Murphy, Padilla et al. 2009, Villasenor, Kalaidzidis et al. 2016). We also found that
508 internalization of DDR-2 at the utse-seam connection correlated with the assembly of type IV
509 collagen at the BM-BM linkage and was dependent on type IV collagen deposition. Type IV
510 collagen is ~400 nm in length and the utse-seam connecting matrix spans spans ~100 nm,
511 while the utse and seam BMs are each ~50 nm thick (Timpl, Wiedemann et al. 1981, Vogel and
512 Hedgecock 2001). Thus, collagen molecules in the connecting matrix could project into the utse
513 and seam BMs to interact with DDR-2 on cell surfaces. Consistent with this possibility, super-
514 resolution imaging of the mouse kidney glomerular basement membrane (GBM), a tissue
515 connection between podocytes and endothelial cells, showed type IV collagen within the GBM
516 projecting into the podocyte and endothelial BMs (Suleiman, Zhang et al. 2013, Naylor, Morais
517 et al. 2021). As DDR-2 is activated by ligand-induced clustering of the receptor (Juskaite,
518 Corcoran et al. 2017, Corcoran, Juskaite et al. 2019), it suggests that the BM-BM linking type IV
519 collagen network, which is specifically assembled at high levels, clusters and activates DDR-2 in
520 the utse and seam cells to coordinate cell-matrix adhesion at the tissue linkage site.
521
522 Vertebrate DDRs can promote integrin mediated cell-matrix adhesion in a variety of cell types.
523 For example, overexpression of DDR1 enhances integrin matrix adhesion in human embryonic
524 kidney cells and in human and mouse fibroblast (Xu, Bihan et al. 2012, Staudinger, Spano et al.
525 2013, Borza, Bolas et al. 2022), and high levels of DDR2 enhances integrin activation in cancer
526 associated fibroblasts in mice (Bayer, Grither et al. 2019). Several mechanisms for DDR-
527 mediated enhancement of integrin adhesion have been proposed, including increased integrin
528 surface levels and Rap1-mediated talin recruitment (Staudinger, Spano et al. 2013, Bayer,

529 Grither et al. 2019). Loss of *C. elegans rap-1* has not been reported to have a Rup/uterine
530 prolapse phenotype (Frische, Pellis-van Berkel et al. 2007) and we found that DDR-2 did not
531 promote talin recruitment to the utse-seam connection. DDR-2 did, however, increase the levels
532 of the two *C. elegans* α integrins—INA-1 and PAT-2—at the utse-seam linkage (Clay and
533 Sherwood 2015), as well as the integrin activating protein DEB-1/vinculin (Bays and DeMali
534 2017). Supporting a functional role for DDR-2 in promoting INA-1 mediated utse-seam
535 attachment, *ddr-2* null mutants strongly enhanced the utse-seam detachment and uterine
536 prolapse defect (Rup phenotype) of animals with reduced INA-1 function. Further, like DDR-2,
537 we found that INA-1 was expressed in the utse and seam cells and through tissue-specific
538 expression of a dominant negative integrin, we determined that integrin activity is required in
539 both tissues to promote adhesion. To understand how DDR-2 affects the strength of INA-1
540 mediated utse-seam adhesion, we performed photobleaching experiments on endogenously
541 tagged INA-1::mNG, and discovered that DDR-2 stabilizes INA-1-mediated adhesion. Through
542 genetic interaction studies, RNAi, and expression of constitutively active Ras (*C. elegans* LET-
543 60), we provide evidence that DDR-2 signals through Ras to promote INA-1 stability. Ras
544 GTPases are a key downstream mediator of DDR signaling (Chen, Kong et al. 2021). Ras has
545 been implicated in activating integrins via a poorly understood mechanism that may involve
546 integrin receptor trafficking (Zhang, Vuori et al. 1996, Conklin, Ada-Nguema et al. 2010, Sandri,
547 Caccavari et al. 2012). Interestingly, expression of the constitutively active form of Ras further
548 increased INA-1 stability at the utse-seam linkage and led to a highly penetrant utse-seam
549 detachment defect. Notably, our photobleaching experiments showed that there was a wide
550 range of integrin stability at the utse-seam attachment site in wild-type animals, likely reflecting
551 low to high adhesion strength. However, Ras activation narrowed integrin to within a high
552 stability range (i.e. high adhesion strength), while *ddr-2* loss as well as Ras reduction shifted
553 integrin towards a narrow, low stability range (low adhesion strength). Together, our
554 observations suggest that DDR-2 signaling through Ras facilitates an increased range of

integrin adhesion at the utse-seam connection, which is required to maintain the utse-seam linkage.

The utse-seam adhesion at the BM-BM tissue linkage is built in the L4 larval stage and then maintained in the adult to support egg-laying (Gianakas, Keeley et al. 2023). Our evidence indicates that DDR-2 activity is highest and perhaps only required between the mid and late L4 larval stages (~four-hour period), as the utse-seam detachment defect peaked by the mid-to-late L4 stage and did not worsen at the late L4 and young adult stages. This timing aligns with a spike in DDR-2 levels in the utse and seam cells and is also when DDR-2 most strongly promoted INA-1 integrin and vinculin levels at the utse-seam linkage. It is possible that DDR-2 is specifically required between the mid and late L4 stages to facilitate a wide range of integrin adhesion. This could adjust the cell-matrix adhesion strength as the BM-BM connecting matrix assembles, strengthens, and changes composition during this time window, shifting from a hemicentin and fibulin-rich to a type IV collagen-dominated matrix (Gianakas, Keeley et al. 2023). Alternatively, a range of integrin adhesion strength may be required to maintain the utse-seam linkage, while allowing the utse and seam to undergo morphogenetic changes to form the tongue (utse) and groove (seam) morphology that secures the tissue linkage. Collectively, our findings support the idea that although the ligands for DDRs are stable collagen molecules, DDRs can function as dynamic sensors of the external environment, allowing cells and tissues to coordinate their activities with changes to the extracellular surroundings.

581 **Materials and Methods**

582 **Key resources table**

Reagent type (species) or resource	**Designation**	**Source or reference**	**Identifiers**	**Additional information**
Strain, strain background (*C. elegans*)	NK2617	(Gianakas, Keeley et al. 2023)		*qyIs23 [cdh-3p::mCh::PH]* II*; lqIs80 [scmp::GFP::CAAX]* IV
Strain, strain background (*C. elegans*)	N2	Caenorhabditis Genetics Center (CGC)		Wild type (ancestral)
Strain, strain background (*C. elegans*)	RB970			*ddr-1(ok874)* X
Strain, strain background (*C. elegans*)	VH1387	(Unsoeld, Park et al. 2013)		*ddr-1(tm382)* X
Strain, strain background (*C. elegans*)	RB788			*ddr-2(ok574)* X
Strain, strain background (*C. elegans*)	VH1383	(Unsoeld, Park et al. 2013)		*ddr-2(tm797)* X

Strain, strain background (*C. elegans*)	NK2511	This study		*ddr-2(qy64)* X
Strain, strain background (*C. elegans*)	NK2655	This study		*qyIs23 [cdh-3p::mCh::PH]* II*; lqIs80 [scmp::GFP::CAAX]* IV; *ddr-2(qy64)* X
Strain, strain background (*C. elegans*)	NK2640	This study		*qy91 [nas-22p::2xmKate2::PH*] II; *lqIs80* [*scmp::GFP::CAAX*] IV
Strain, strain background (*C. elegans*)	NK2682	This study		*qy91 [nas-22p::2xmKate2::PH]* II; *lqIs80 [scmp::GFP::CAAX]* IV; *ddr-2(qy64)* X
Strain, strain background (*C. elegans*)		This study		*qy44 [ddr-2::mNG]* X; *qyEx605 [scmp::2xmKate2:PH]*

Strain, strain background (*C. elegans*)	NK2620	This study		*qyIs23 [cdh-3p::mCh::PH]* II*; qy44 [ddr-2::mNG]* X
Strain, strain background (*C. elegans*)	NK2763	This study		*qyIs256 [cdh-3p::mCherry::rab-5]* ?; *qy44 [ddr-2::mNG*] X
Strain, strain background (*C. elegans*)	NK2766	This study		*qyIs252 [cdh-3p::mCherry::rab-7]* ?; *qy44 [ddr-2::mNG*] X
Strain, strain background (*C. elegans*)	NK2769	This study		*qyIs205 [cdh-3p::mCherry::rab-11]* ?; *qy44 [ddr-2::mNG*] X
Strain, strain background (*C. elegans*)	NK2901	This study		*qy188 [scmp::mKate2::rab-5]* I; *qy44 [ddr-2::mNG*] X
Strain, strain background (*C. elegans*)	NK2926	This study		*qy91 [nas-22p::2xmKate2::PH*] II; *IqIs80* [*scmp::GFP::CAAX*] IV; *ddr-2(ok574)* X

Strain, strain background (*C. elegans*)	NK2705	(Jayadev, Morais et al. 2022)		*qy118 [col-99::mNG (internal tag)]* IV
Strain, strain background (*C. elegans*)	NK2322	(Keeley, Hastie et al. 2020)		*qy22 [cle-1::mNG]* I
Strain, strain background (*C. elegans*)	NK2326	(Keeley, Hastie et al. 2020)		*qy24 [emb-9::mNG (internal tag)]* III
Strain, strain background (*C. elegans*)	NK2830	This study		*qy166 [cdh-3p::dominant negative ddr-2::mNG]* I; *qy91 [nas-22p::2xmKate2::PH]* II; *heIs63 [wrt-2p::GFP::PH + wrt-2p::GFP::H2B + lin-48p:mCherry]* V
Strain, strain background (*C. elegans*)	NK2848	This study		*qy175 [scmp::dominant negative ddr-2::mKate2]* I; *qy91 [nas-22p::2xmKate2::PH]*

				II; *heIs63 [wrt-2p::GFP::PH + wrt-2p::GFP::H2B + lin-48p:mCherry]* V
Strain, strain background (*C. elegans*)	NK2585	(Jayadev, Morais et al. 2022)		*qy83 [emb-9::mRuby2 (internal tag)]* III
Strain, strain background (*C. elegans*)	NK2422	(Keeley, Hastie et al. 2020)		*qy33 [him-4::mNG]* X
Strain, strain background (*C. elegans*)	NK2324	(Jayadev, Chi et al. 2019)		*qy23 [ina-1::mNG]* III
Strain, strain background (*C. elegans*)	NK2479	(Jayadev, Chi et al. 2019)		*qy49 [pat-2::2xmNG]* III
Strain, strain background (*C. elegans*)	NK2825	This study		*qy23 [ina-1::mNG]* III; *ddr-2(qy64)* X
Strain, strain background (*C. elegans*)	NK2858	This study		*qy49 [pat-2::2xmNG]* III; *ddr-2(qy64)* X
Strain, strain background (*C. elegans*)	NK2804	This study		*qyIs23 [cdh-3p::mCh::PH]* II; *heIs63 [wrt-*

				2p::GFP::PH + wrt-2p::GFP::H2B + lin-48p:mCherry] V
Strain, strain background (*C. elegans*)	NK2824	This study		*qyIs23 [cdh-3p::mCh::PH]* II; *qyIs15 [zmp-1$^{mk50-51}$p::dominant negative integrin b-pat-3]* IV;*heIs63 [wrt-2p::GFP::PH + wrt-2p::GFP::H2B + lin-48p:mCherry]* V
Strain, strain background (*C. elegans*)	NK2934	This study		*qy91 [nas-22p::2xmKate2::PH*] II; *unc-119(ed4)* III; *IqIs80* [*scmp::GFP::CAAX*] IV; *qyEx604 [wrt-2p::dominant negative integrin b-pat-3 + unc-119(+)]*
Strain, strain background (*C. elegans*)	NK2579	(Keeley, Hastie et al. 2020)		*qy62 [mNG::fbl-1] IV*

Strain, strain background (*C. elegans*)	NK932	(Kelley, Chi et al. 2019)		*qyIs190 [zmp-4p::zmp-4::GFP]*
Strain, strain background (*C. elegans*)	NK268	(Hagedorn, Yashiro et al. 2009)		*qyIs17 [zmp-1$^{mk50-51}$p mCherry]*
Strain, strain background (*C. elegans*)	AH3437	(Walser, Umbricht et al. 2017)		*zh117 [GFP::tln-1]* I
Strain, strain background (*C. elegans*)	NK2478	This study		*qy48 [deb-1::mNG]* IV
Strain, strain background (*C. elegans*)	NK2854	This study		*zh117 [GFP::tln-1]* I; *ddr-2(qy64)* X
Strain, strain background (*C. elegans*)	NK2860	This study		*qy48 [deb-1::mNG]* IV; *ddr-2(qy64)* X
Strain, strain background (*C. elegans*)	NK2944	This study		*qy91 [nas-22p::2xmKate2::PH*] II; *lqIs80* [*scmp::GFP::CAAX*] IV; *let-60(qy203)* IV

Strain, strain background (*C. elegans*)	NK2957	This study		*qy23 [ina-1::mNG]* III; *let-60(qy203)* IV
Strain, strain background (*E. coli*)	*emb-9* RNAi	(Kamath and Ahringer 2003)		Clone from Ahringer library (L4440 vector backbone)
Strain, strain background (*E. coli*)	*col-99* RNAi	(Rual, Ceron et al. 2004)		Clone from Vidal library (L4440 vector backbone)
Strain, strain background (*E. coli*)	*cle-1* RNAi	(Rual, Ceron et al. 2004)		Clone from Vidal library (L4440 vector backbone)
Strain, strain background (*E. coli*)	*ina-1* RNAi	(Rual, Ceron et al. 2004)		Clone from Vidal library (L4440 vector backbone)
Strain, strain background (*E. coli*)	*let-60* RNAi	(Rual, Ceron et al. 2004)		Clone from Vidal library (L4440 vector backbone)
Strain, strain background (*E. coli*)	*deb-1* RNAi	(Rual, Ceron et al. 2004)		Clone from Vidal library (L4440 vector backbone)
Strain, strain background (*E. coli*)	*him-4* RNAi	(Gianakas, Keeley et al. 2023)		T444t vector backbone

Strain, strain background (*E. coli*)	*ddr-2* RNAi	This study		T444t vector backbone
Sequence-based reagent	*ddr-2* knockout (*ddr-2(qy64)*) sgRNA 1	This study		ATCCTGACATAGA TGAGCGT
Sequence-based reagent	*ddr-2* knockout (*ddr-2(qy64)*) sgRNA 2	This study		GTCATTGGTGCAC ACTTCTC
Sequence-based reagent	*ddr-2* knockout (*ddr-2(qy64)*) sgRNA 3	This study		AAGTGTGCACCAA TGACTGG
Sequence-based reagent	*deb-1::mNG* (*deb-1(qy48)*) sgRNA 1	This study		AGTTGGACCACAT TGGCTTT
Sequence-based reagent	*deb-1::mNG* (*deb-1(qy48)*) sgRNA 2	This study		ATTTAGAAGTTGG ACCACAT
Sequence-based reagent	*let-60* gain-of-function (*let-60(qy203)*) sgRNA 1	This study		CTTGTGGTAGTTG GAGATGG
Sequence-based reagent	Primer *ddr-2(qy64)* homology arm forward	This study		TTTTCAGAGTCTC CGACGCTCATCTA

Sequence-based reagent	Primer *ddr-2(qy64)* homology arm reverse	This study		TAAATATTATTCTG AGAATATA
Sequence-based reagent	Primer *ddr-2(qy64)* genotyping forward	This study		TGGTAATTGATGA GAGGGTG
Sequence-based reagent	Primer *ddr-2(qy64)* genotyping reverse	This study		TGTCGTTTCGACA CCGGCAA 1.8 kb band
	Primer *let-60(qy203)* homology arm forward	This study		ATGACGGAGTACA AGCTTGTGGTAGT TGGAGATGGAGA AGT
	Primer *let-60(qy203)* homology arm reverse	This study		TACCCTTTTCTGA AAAAAGACGC
Sequence-based reagent	Primer *nas-22* promoter forward	This study		TCAAAGCGTCAAG CTTTACG

Sequence-based reagent	Primer *nas-22* promoter reverse	This study		TTTTCTGTCTACAAGGACTGTGC
Sequence-based reagent	Primer *scm* promoter forward	(Chapman, Li et al. 2008)		AACCTCCACCAGATGGTTGGCG
Sequence-based reagent	Primer *scm* promoter reverse	(Chapman, Li et al. 2008)		CCCGGGGATCCGTCCACTCT
Sequence-based reagent	Primer *cdh-3* promoter forward	This study		CTAGAGCATGATGTCCTTAC
Sequence-based reagent	Primer *cdh-3* promoter reverse	This study		CAAAACGGACCGACCGTCCC
Sequence-based reagent	Primer *dominant negative ddr-2* forward	This study		ATGAAGTTGCTGCTGTATCT
Sequence-based reagent	Primer *dominant negative ddr-2* reverse	This study		TCTGCTCACGCAAATCAACT

Sequence-based reagent	Primer *wrt-2* promoter forward	This study		TCAGAACTCTAATACTTACT
Sequence-based reagent	Primer *wrt-2* promoter reverse	This study		CCGAGAAACAATTGGCAGGT
Sequence-based reagent	Primer *dominant negative integrin b pat-3* forward	(Hagedorn, Yashiro et al. 2009)		TCTAGAGGATCCCGGGGAT
Sequence-based reagent	Primer *dominant negative integrin b pat-3* reverse	(Hagedorn, Yashiro et al. 2009)		ATTTAGTTGGCTTTTCCAGC
Sequence-based reagent	Primer *ddr-2* RNAi forward	This study		ATGAAGTTGCTGCTGTATCT
Sequence-based reagent	Primer *ddr-2* RNAi reverse	This study		ATGAATATGAGGAGAAGTGTGC
Recombinant DNA reagent	Plasmid: pCFJ352	Addgene	RRID: Addgene_30539	sgRNA targeting MosSCI insertion

				site on Chr I, from Erik Jorgensen
Recombinant DNA reagent	Plasmid: pDD122	(Dickinson, Ward et al. 2013)	RRID: Addgene_47550	sgRNA targeting MosSCI insertion site on Chr II
	Plasmid: pAP087	(Pani and Goldstein 2018)		starter SEC repair template plasmid for single copy insertion at the ttTi5605 site on chromosome II
Recombinant DNA reagent	Plasmid: pAP088	(Pani and Goldstein 2018)		starter SEC repair template plasmid for single copy insertion at the ttTi4348 site on chromosome I
Chemical compound, drug	Ampicillin	Sigma-Aldrich	#A0166	
Chemical compound, drug	Isopropyl β-D-1-thiogalactopyranoside	Sigma-Aldrich	#I6758	
Chemical compound, drug	Hygromycin B	Sigma-Aldrich	#H3274	
Chemical compound, drug	Sodium azide	Sigma-Aldrich	#S2002	

Chemical compound, drug	Levamisole	Sigma-Aldrich	#L9756	
Software, algorithm	µManager v.1.4.23			
Software, algorithm	Zen Black			
Software, algorithm	Fiji/ImageJ			
Software, algorithm	GraphPad Prism v9			

583

584 ***C. elegans* culture and strains**

585 *C. elegans* strains used in this study are listed in the ***Key resources table***. Worms were reared
586 on nematode growth medium plates seeded with OP50 *Escherichia coli* at 16°C, 18°C, or 20°C
587 according to standard procedures (Stiernagle 2006). We used *C. elegans* vulval development to
588 accurately stage animals through the morphogenesis of the utse-seam connection (late L3 to
589 young adult stage) (Mok, Sternberg et al. 2015).

590

591 **Generation of genome-edited strains**

592 To generate the genome-edited mNeonGreen (mNG) knock-in allele for *deb-1* (*qy48*), we used
593 CRISPR/Cas9 genome editing with a self-excising cassette (SEC) for drug selection
594 (hygromycin treatment) as described previously (Dickinson, Ward et al. 2013, Keeley, Hastie et
595 al. 2020). An 18 amino acid flexible linker attached to the mNG fluorophore was inserted in
596 frame and directly upstream of the stop codon. sgRNA sequences directing Cas9 cleavage near
597 the C-terminus are provided in the ***Key resources table***.

598

599 The *ddr-2* knockout allele *ddr-2(qy64)*, an 8615 bp deletion corresponding to the coding
600 sequence of DDR-2, was also generated with the SEC CRISPR method detailed above with one
601 modification—we generated a new starter repair plasmid lacking the fluorescent tag. Primers
602 used to amplify homology arms, sgRNA sequences to direct Cas9 cleavage, and genotyping
603 primers used to verify genome-edited knockout animals are provided in the ***Key resources***
604 ***table***.
605
606 For the LET-60^{G13E} gain-of function mutation, *let-60(qy203)*, we used the same strategy as the
607 *ddr-2* knockout allele. The point mutation was incorporated into the primer for homology arm
608 amplification. Note that this mutation is identical to the *let-60(n1046)* allele.
609
610 **Generation of transgenic strains**
611 For the utse marker *qy91 [nas-22p::2xmKate2::pH]*, we generated a single-copy transgene
612 inserted into the ttTi5605 transposon insertion on chromosome II (Frokjaer-Jensen, Davis et al.
613 2012) using the SEC CRISPR method detailed above. A 2 kb *nas-22* promoter, two tandem
614 mKate2 fluorophores attached to a PH domain, and an *unc-54* 3' UTR fragment were ligated in
615 order via Gibson assembly into the pAP087 starter repair plasmid containing homology arms for
616 the ttTi5605 site. The sgRNA directing Cas9 cleavage near this region is contained in the
617 pDD122 vector.
618
619 To express mKate2-tagged RAB-5 in the seam, we generated a single-copy transgene inserted
620 into the ttTi4348 transposon insertion site on chromosome I (Frokjaer-Jensen, Davis et al. 2012)
621 using SEC CRISPR. Briefly, the scm promoter, mKate2 fluorophore, rab-5 genomic sequence,
622 and *unc-54* 3' UTR were Gibson assembled in order into the pAP088 starter repair plasmid
623 containing homology arms for the ttTi4348 site. The sgRNA directing Cas9 cleavage near this
624 region is contained in the pCFJ352 vector.

625

626 For tissue-specific expression of dominant negative (DN) DDR-2 in the utse or seam, we also
627 generated single-copy transgenes inserted into the ttTi4348 site. For utse expression, the
628 following fragments were Gibson assembled in order into pAP088: a 1.5kb *cdh-3* promoter
629 fragment, *DN ddr-2*, mNG fluorophore, and *unc-54* 3' UTR. Expression in transgenic animals
630 was verified by assessing mNG fluorescence. For seam expression, the following fragments
631 were Gibson assembled in order into pAP088: the *scm* promoter fragment, *DN ddr-2*, and
632 mKate2 fluorophore. Expression in transgenic animals was verified by assessing mKate2
633 fluorescence.

634

635 The seam cell marker *qyEx605 [scmp::2xmKate2::PH]* was built by Gibson assembling a 1.3 kb
636 *scm* promoter fragment, a fragment with two tandem mKate2 fluorophores attached to the PH
637 domain, and *unc-54* 3' UTR fragment in order. The construct was expressed as
638 extrachromosomal arrays as described previously (Yochem and Herman 2003).

639

640 To build the construct for *DN integrin* expressed in the seam, we first amplified the *DN integrin*
641 fragment from animals harboring the *qyIs15* allele (see ***Key resources table***). The *DN integrin*
642 fragment is composed of a *pes-10* enhancer element, the *ost-1* signal peptide, the *pat-3* β-tail
643 fragment, and *unc-54* 3' UTR as described previously (Lee Cram et al. 2001). The *DN integrin*
644 fragment was fused to a 1.3 kb *wrt-2* promoter by PCR. The construct was expressed
645 extrachromosomally.

646

647 **RNAi**

648 All RNAi constructs except for *ddr-2* RNAi were obtained from the Ahringer and Vidal RNAi
649 libraries (Kamath and Ahringer 2003, Rual, Ceron et al. 2004) or generated previously
650 (Gianakas, Keeley et al. 2023). For the *ddr-2* clone, a ~2.4 kb cDNA fragment corresponding to

651 the longest *ddr-2* transcript was amplified by PCR and inserted into the T444t vector as
652 described previously (Gianakas et al 2023). RNAi experiments were performed using the
653 feeding method (Timmons, Court et al. 2001) according to previously detailed protocols
654 (Jayadev, Chi et al. 2019, Gianakas, Keeley et al. 2023). For experiments assessing the utse-
655 seam connection, RNAi was initiated in synchronized L1 larvae and animals were examined at
656 the late L4 stage (~ 44 h treatment). For examination of uterine prolapse, RNAi was performed
657 from the L1 through adulthood (~ 120 h treatment). For depletion of hemicentin initiated at the
658 early L4 stage, synchronized L1 worm were grown on control RNAi for ~ 38 h to the early L4,
659 and then transferred onto *him-4* RNAi to the late L4 (~5-6 h treatment). We verified knockdown
660 efficiencies for all RNAi experiments except for *let-60* RNAi by including a control with the
661 relevant fluorescent tagged target protein, achieving between ~75 to 100% reduction. We
662 verified *let-60* RNAi knockdown efficiency by plate level assessment of brood size, which was
663 strongly reduced compared to control animals, as previously reported (Ceron, Rual et al. 2007).
664

665 **Microscopy and image processing**

666 All fluorescence images (except for photobleaching experiments) were acquired at 20°C on
667 Zeiss Axio Imager A1 microscopes controlled by the μManager software v.1.4.23 or v.2.0.1
668 (Edelstein, Amodaj et al. 2010), equipped with a Hamamatsu ImagEM electron multiplying
669 charge-coupled device camera or an Orca-Fusion scientific complementary metal oxide
670 semiconductor camera, Zeiss 40x and 100x Plan Apochromat (1.4 numerical aperture) oil
671 immersion objectives, Yokogawa CSU-10 spinning disc confocal scan heads, and 488 nm, 505
672 nm, and 561 nm laser lines. Worms were mounted on 5% noble agar pads containing 0.01M
673 sodium azide for imaging.
674

675 For photobleaching experiments, images were acquired at 20°C on a Zeiss 880 single-point
676 scanning confocal attached to a Zeiss Axio Observer Z1 microscope, with a Marzhauser linearly

677 encoded stage, a 40x Plan Neofluar (1.3 numerical aperture) oil immersion objective, and a 488
678 nm laser line. Worms were anesthetized by soaking in 5 mM levamisole in M9 buffer for 15 min
679 and then transferred to 4% noble agar pads. Coverslips were then placed and sealed on top
680 with valap (equal weight Vaseline, lanolin, and paraffin) and flooded with 5 mM levamisole.
681 Coverslip sealing kept the animals hydrated during the experimental timeframe, ensuring
682 accurate imaging of endogenous protein dynamics (detailed in (Kelley, Wang et al. 2017)). A
683 rectangle region within one arm of the BM-BM connection BLINK was photobleached using 30
684 iterations of simultaneous 405 nm and 488 nm excitation at 100% laser power for a total
685 bleaching time of 1.5 seconds. Worms were imaged prior and immediately following bleaching,
686 and then again 10 min later.
687
688 Brightfield images of worms were acquired at 20°C on a Zeiss Axio Zoom V16 stereo
689 fluorescence microscope controlled by Zen 3.2 software, equipped with an Axiocam digital
690 camera and a 3x objective. Worms were imaged without immobilization.
691
692 To image the utse and seam cells ventrally, we manually oriented animals in the ventral
693 orientation (Kelley, Wang et al. 2017) and acquired z-stacks at 0.37 μm intervals, capturing the
694 entire H-shaped structure of the utse and the seam cells flanking both sides of the utse at 100x
695 magnification. Ventral views of the utse and seam shown in figures are maximum intensity
696 projections of these z-stacks. 3D isosurface renderings of the utse and seam cells shown in
697 ***Figure 2D*** were generated with Imaris 7.4 software (Bitplane). We acquired lateral z-stacks at
698 0.37 μm intervals to fully capture the superficial half of the utse-seam attachment.
699
700 For lateral imaging of DDR-2::mNG together with the utse, seam cells, or endosome markers
701 expressed in the utse or seam, we acquired z-stacks at 0.37 μm intervals to capture as much of
702 each tissue that was in focus superficially at 40x magnification. Images shown in figures are

703 single slices where DDR-2 was sharply in focus within the tissue of interest. The same
704 parameters were used for imaging INA-1::mNG and PAT-2::mNG in the utse and seam. Images
705 in ***Figure 5A*** correspond to the z-slices where INA-1 and PAT-2 were most in focus at the BM-
706 BM connection region. In ***Figure 5—figure supplement 2A and B***, images shown are sum
707 projections of the seam or utse regions.
708
709 To image DDR-2::mNG specifically at the utse-seam attachment site, we acquired lateral z-
710 stacks at 0.37 µm intervals capturing both the surface of the utse and the seam cells. We used
711 a utse cell marker as a reference to accurately capture this region (see also schematic in ***Figure***
712 ***3A***). Images shown in ***Figure 4*** are sum projections of these z-stacks.
713
714 For lateral imaging of respective tagged proteins at the BM-BM connection region, we acquired
715 single slices (40x magnification) at the middle focal plane where the BM-BM connection signal
716 was sharply in focus. All images were process in Fiji 2.0 (Schindelin, Arganda-Carreras et al.
717 2012).
718
719 **Image analysis and quantification**
720 To assess utse-seam detachment, we used maximum intensity projections of the utse and
721 seam viewed ventrally as detailed above. We defined utse-seam detachment as any gap in the
722 utse-seam attachment of at least 4 square pixels in area. We preferred the ventral view over 3D
723 rendering for this metric as gaps were variable in size and location (typically occurring in one or
724 two arms of the utse on opposite sides). The ventral projections allowed us to reliably examine
725 all four arms of the utse and whether they were in contact with the seam from animal to animal.
726 The visual representation of a gap in a ventral maximum projection is an underestimate of the
727 true size of the detachment, as the tongue-in-groove association of the utse and seam can only
728 be seen in a 3D surface rendering of the utse and seam viewed from the side. We thus used a

729 binary scoring system (animals with or without utse-seam detachments) instead of quantifying
730 the size of the detached region. We note that ventral imaging of the utse and seam sometimes
731 results in small utse-seam detachments as we manually orient the animals on the slide. To
732 control for this, we acquired large datasets (at least 40 animals examined) for every control
733 strain we used to visualize the utse-seam attachment with. We found that small detachments
734 related to ventral imaging occurred in ~8-12% of animals, depending on the genetic
735 background. All datasets shown in figures have been normalized to account for this.
736
737 All quantifications of mean fluorescence intensity were done on raw images in Fiji 2.0. We drew
738 ~5-pixel long and 2-pixel wide linescans to obtain raw values of mean fluorescence intensity.
739 We measured mean fluorescence intensity for all quantifications in order to account for linescan
740 area. For measurement within the BM-BM connection region, we positioned the linescan within
741 the arm that was most in focus. Other regions where linescans were performed are indicated in
742 figures. Background intensity values were obtained with similar linescans in adjacent regions
743 with no visible fluorescence signal. Note that we used two tandem mNG fluorophores to
744 visualize PAT-2 at the utse-seam attachment site (PAT-2::2xmNG) as it was present at very low
745 levels. We imaged PAT-2::mNG and PAT-2::2xmNG in this region at the same exposure and
746 found that the latter was approximately two times brighter (PAT-2::2xmNG mean fluorescence
747 intensity 3941 ± 847 A.U., PAT-2::mNG 2037 ± 465 A.U., n = 10 animals examined each).
748 Taken together with quantifications in ***Figure 5B***, INA-1 is thus likely present at six-fold higher
749 levels than PAT-2 at the utse-seam attachment site. For additional quantification related to
750 FRAP, see below.
751
752 For FRAP analysis, we measured mean fluorescence intensity within the bleached region. In
753 addition, we performed an equivalent linescan within the unbleached arm at the BM-BM
754 connection to calculate a bleach correction factor to account for general photobleaching during

755 image acquisition across the duration of the experiment, as previously described (Gianakas,
756 Keeley et al. 2023). Briefly, the background-corrected fluorescence intensity measurement on
757 the side of the BM-BM connection where FRAP was not performed at the 10 min post-bleach
758 timepoint was divided by the respective value at the pre-bleach timepoint to obtain the bleach
759 correction factor. Fluorescence intensity measurements at the pre-bleach and post-bleach
760 timepoints on the side of the BM-BM connection where FRAP was performed were then
761 multiplied by the respective bleach correction factor to normalize these values to the 10 min
762 post-bleach fluorescence intensity measurement in the same region.
763
764 To count the number of DDR-2 punctae at the site of utse-seam attachment, we used sum
765 projections of DDR-2::mNG capturing the surface of the utse and seam (described earlier). We
766 restricted measurements to the utse-seam connection corresponding to one utse arm.
767 Brightness and contrast was then adjusted to manually count individual punctae, as DDR-2
768 punctae showed a large variance in size and fluorescence intensity. Note that in the type IV
769 collagen depletion condition, we only counted discrete puncta and did not include the large cell
770 surface accumulation of DDR-2 in the analysis.
771
772 To determine co-localization of DDR-2 with markers of endocytic vesicles, we also used a
773 manual approach due to the large variability of the size and fluorescence intensity of punctae.
774 We selected a single slice where the utse or the seam was sharply in focus, and restricted
775 measurements to a single utse arm or a region of the seam corresponding to a single utse arm.
776 For each animal, the number, and positions of DDR-2 punctae were noted and compared to the
777 respective endosome marker (RAB-5, RAB-7, or RAB-11). If a DDR-2 puncta physically
778 overlapped with or was in contact with an endosome punctum, it was classified as one that co-
779 localized with the endosomal marker. We then calculated the percentage overlap of DDR-2

780 punctae with the vesicle marker for each animal (corresponding to each data point within
781 boxplots in ***Figure 3—figure supplement 1B and C***).
782
783 **Scoring of uterine prolapse**
784 Uterine prolapse frequency was assessed as described previously (Gianakas, Keeley et al.
785 2023). Briefly, synchronized L1 larvae were plated (~20 animals per plate) and after 24 h, the
786 exact number of worms on each plate was recorded. Plates were then visually screened for
787 ruptured worms (uterine prolapse) every 24 h during egg-laying (between 48 h to 120 h post-
788 L1). We chose to examine the entire egg-laying period as ruptures arising from utse-seam
789 detachments do not usually occur at the onset of egg-laying, but after cycles of egg-laying that
790 place repeated mechanical stress on the utse-seam connection (Gianakas, Keeley et al. 2023).
791 Ruptured animals were scored and removed from plates to avoid double counting and after 120
792 h, the percentage of animals with uterine prolapse was calculated. At least 50 animals were
793 screened for every experiment.
794
795 **Illustrations of utse-seam tissue connection**
796 For schematics in Figure 1A and Figure 8, model protein sizing was scaled according to
797 previously generated models (Keeley, Hastie et al. 2020). We sized hemicentin, fibulin, type IV
798 collagen, integrin, and DDR-2. We also approximated the span of the basement membranes of
799 the utse and seam cells (~50 nm each), as well as the BM-BM connecting matrix (~200 nm),
800 based on electron microscopy of the utse-seam attachment (Vogel and Hedgecock 2001).
801
802 **Statistical analysis**
803 Statistical analysis was performed in GraphPad Prism 9. Normality of datasets was assessed
804 using the D'Agostino-Pearson normality test. We used parametric tests for datasets that
805 followed a Gaussian distribution and non-parametric tests for those that did not. For

806 comparisons of means between two populations, we used either an unpaired two-tailed
807 Student's *t* test or a Mann-Whitney *U* test. For comparisons of means between three or more
808 populations, we performed either a one-way ANOVA followed by post hoc Dunnett's test or
809 Kruskal-Wallis *H* test with post hoc Dunn's test. For comparisons between two categorical
810 variables, we used the Fisher's exact test. All graphs were prepared in GraphPad Prism. Figure
811 legends indicate sample sizes, statistical tests used, and *P* values.
812

813 **Data availability**

814 All data generated in this study are included in the manuscript and supporting files.
815

816 **Acknowledgements**

817 We would like to thank C. Borza, A. Pozzi, B. Hoffman, and D. Reiner for helpful discussions, C.
818 Gianakas for comments on the manuscript, and M. Boxem and H. Hutter for strains. Some
819 strains were provided by the CGC, which is funded by NIH Office of Research Infrastructure
820 Programs (P40 OD010440). S.G.P. was supported by graduate research fellowship NICHD F31
821 HD97901. This work was supported by R35GM118049, R21OD028766, and R21OD032430 to
822 D.R.S.
823
824
825
826
827
828
829
830

Additional Information

Funding

Funder	Grant reference number	Author
National Institutes of Health	R35GM118049	David R. Sherwood
National Institutes of Health	R21OD028766	David R. Sherwood
National Institutes of Health	R21OD032430	David R. Sherwood
National Institute of Child Health and Human Development	F31 HD97901	Sara G. Payne

Author Contributions

Kieop Park, conceptualization, data curation, formal analysis, investigation, visualization, methodology, writing-original draft; Ranjay Jayadev, conceptualization, data curation, formal analysis, investigation, visualization, methodology, writing-original draft; Sara G. Payne, Conceptualization, data curation, formal analysis, investigation, visualization, methodology, writing-original draft, funding acquisition; Isabel W. Kenny-Ganzert, investigation, methodology; Qiuyi Chi, investigation, methodology; Daniel S. Costa, methodology; William Ramos-Lewis, investigation, methodology; Siddharthan Balachandar Thendral, visualization; David R. Sherwood, supervision, writing-original draft, funding acquisition, project administration.

Competing Interests

No competing interests declared for all authors

Author ORCID

Kieop Park https://orcid.org/0000-0002-6380-4730

Ranjay Jayadev https://orcid.org/0000-0003-0465-0337

Sara G. Payne https://orcid.org/0000-0002-3572-9112

Isabel Kenny-Ganzert https://orcid.org/0000-0001-6306-4472

Qiuyi Chi https://orcid.org/0000-0003-1297-4163

Daniel S. Costa https://orcid.org/0000-0003-2179-8800

Will Ramos-Lewis https://orcid.org/0000-0002-4627-4571

Siddharthan Balachandar Thendral https://orcid.org/0000-0002-4674-7033

David R Sherwood https://orcid.org/0000-0002-4448-6917

887 **References**
888
889 Abrahamson, D. R. (1985). "Origin of the glomerular basement membrane visualized after in
890 vivo labeling of laminin in newborn rat kidneys." J Cell Biol **100**(6): 1988-2000.
891 Altincicek, B., M. Fischer, M. Fischer, K. Luersen, M. Boll, U. Wenzel and A. Vilcinskas (2010).
892 "Role of matrix metalloproteinase ZMP-2 in pathogen resistance and development in
893 Caenorhabditis elegans." Dev Comp Immunol **34**(11): 1160-1169.
894 Bayer, S. V., W. R. Grither, A. Brenot, P. Y. Hwang, C. E. Barcus, M. Ernst, P. Pence, C. Walter,
895 A. Pathak and G. D. Longmore (2019). "DDR2 controls breast tumor stiffness and metastasis by
896 regulating integrin mediated mechanotransduction in CAFs." Elife **8**.
897 Bays, J. L. and K. A. DeMali (2017). "Vinculin in cell-cell and cell-matrix adhesions." Cell Mol
898 Life Sci **74**(16): 2999-3009.
899 Bernadskaya, Y. Y., S. Brahmbhatt, S. E. Gline, W. Wang and L. Christiaen (2019). "Discoidin-
900 domain receptor coordinates cell-matrix adhesion and collective polarity in migratory
901 cardiopharyngeal progenitors." Nat Commun **10**(1): 57.
902 Borza, C. M., G. Bolas, X. Zhang, M. B. Browning Monroe, M. Z. Zhang, J. Meiler, M. J. Skwark,
903 R. C. Harris, L. A. Lapierre, J. R. Goldenring, M. Hook, J. Rivera, K. L. Brown, B. Leitinger, M. J.
904 Tyska, M. Moser, R. T. Bottcher, R. Zent and A. Pozzi (2022). "The Collagen Receptor Discoidin
905 Domain Receptor 1b Enhances Integrin beta1-Mediated Cell Migration by Interacting With
906 Talin and Promoting Rac1 Activation." Front Cell Dev Biol **10**: 836797.
907 Borza, C. M. and A. Pozzi (2014). "Discoidin domain receptors in disease." Matrix Biol **34**: 185-
908 192.
909 Brown, K. L., C. F. Cummings, R. M. Vanacore and B. G. Hudson (2017). "Building collagen IV
910 smart scaffolds on the outside of cells." Protein Sci **26**(11): 2151-2161.
911 Brown, N. H. (2011). "Extracellular matrix in development: insights from mechanisms
912 conserved between invertebrates and vertebrates." Cold Spring Harb Perspect Biol **3**(12).
913 Carney, T. J., N. M. Feitosa, C. Sonntag, K. Slanchev, J. Kluger, D. Kiyozumi, J. M. Gebauer, J.
914 Coffin Talbot, C. B. Kimmel, K. Sekiguchi, R. Wagener, H. Schwarz, P. W. Ingham and M.
915 Hammerschmidt (2010). "Genetic analysis of fin development in zebrafish identifies furin and
916 hemicentin1 as potential novel fraser syndrome disease genes." PLoS Genet **6**(4): e1000907.
917 Castro-Sanchez, L., A. Soto-Guzman, N. Navarro-Tito, R. Martinez-Orozco and E. P. Salazar
918 (2010). "Native type IV collagen induces cell migration through a CD9 and DDR1-dependent
919 pathway in MDA-MB-231 breast cancer cells." Eur J Cell Biol **89**(11): 843-852.
920 Ceron, J., J. F. Rual, A. Chandra, D. Dupuy, M. Vidal and S. van den Heuvel (2007). "Large-scale
921 RNAi screens identify novel genes that interact with the C. elegans retinoblastoma pathway as
922 well as splicing-related components with synMuv B activity." BMC Dev Biol **7**: 30.
923 Chapman, J. O., H. Li and E. A. Lundquist (2008). "The MIG-15 NIK kinase acts cell-
924 autonomously in neuroblast polarization and migration in C. elegans." Dev Biol **324**(2): 245-257.
925 Chastney, M. R., J. R. W. Conway and J. Ivaska (2021). "Integrin adhesion complexes." Curr Biol
926 **31**(10): R536-R542.
927 Chen, L., X. Kong, Y. Fang, S. Paunikar, X. Wang, J. A. L. Brown, E. Bourke, X. Li and J. Wang
928 (2021). "Recent Advances in the Role of Discoidin Domain Receptor Tyrosine Kinase 1 and

929 Discoidin Domain Receptor Tyrosine Kinase 2 in Breast and Ovarian Cancer." Front Cell Dev
930 Biol **9**: 747314.
931 Clay, M. R. and D. R. Sherwood (2015). "Basement Membranes in the Worm: A Dynamic
932 Scaffolding that Instructs Cellular Behaviors and Shapes Tissues." Curr Top Membr **76**: 337-371.
933 Conklin, M. W., A. Ada-Nguema, M. Parsons, K. M. Riching and P. J. Keely (2010). "R-Ras
934 regulates beta1-integrin trafficking via effects on membrane ruffling and endocytosis." BMC
935 Cell Biol **11**: 14.
936 Corcoran, D. S., V. Juskaite, Y. Xu, F. Gorlitz, Y. Alexandrov, C. Dunsby, P. M. W. French and B.
937 Leitinger (2019). "DDR1 autophosphorylation is a result of aggregation into dense clusters." Sci
938 Rep **9**(1): 17104.
939 Dickinson, D. J., J. D. Ward, D. J. Reiner and B. Goldstein (2013). "Engineering the
940 Caenorhabditis elegans genome using Cas9-triggered homologous recombination." Nat
941 Methods **10**(10): 1028-1034.
942 Edelstein, A., N. Amodaj, K. Hoover, R. Vale and N. Stuurman (2010). "Computer control of
943 microscopes using microManager." Curr Protoc Mol Biol **Chapter 14**: Unit14 20.
944 Feitosa, N. M., J. Zhang, T. J. Carney, M. Metzger, V. Korzh, W. Bloch and M. Hammerschmidt
945 (2012). "Hemicentin 2 and Fibulin 1 are required for epidermal-dermal junction formation and
946 fin mesenchymal cell migration during zebrafish development." Dev Biol **369**(2): 235-248.
947 Fidler, A. L., S. P. Boudko, A. Rokas and B. G. Hudson (2018). "The triple helix of collagens - an
948 ancient protein structure that enabled animal multicellularity and tissue evolution." J Cell Sci
949 **131**(7).
950 Frische, E. W., W. Pellis-van Berkel, G. van Haaften, E. Cuppen, R. H. Plasterk, M. Tijsterman, J.
951 L. Bos and F. J. Zwartkruis (2007). "RAP-1 and the RAL-1/exocyst pathway coordinate
952 hypodermal cell organization in Caenorhabditis elegans." EMBO J **26**(24): 5083-5092.
953 Frokjaer-Jensen, C., M. W. Davis, M. Ailion and E. M. Jorgensen (2012). "Improved Mos1-
954 mediated transgenesis in C. elegans." Nat Methods **9**(2): 117-118.
955 Fu, H. L., R. R. Valiathan, R. Arkwright, A. Sohail, C. Mihai, M. Kumarasiri, K. V. Mahasenan, S.
956 Mobashery, P. Huang, G. Agarwal and R. Fridman (2013). "Discoidin domain receptors: unique
957 receptor tyrosine kinases in collagen-mediated signaling." J Biol Chem **288**(11): 7430-7437.
958 Gao, Y., D. Mruk, H. Chen, W. Y. Lui, W. M. Lee and C. Y. Cheng (2017). "Regulation of the
959 blood-testis barrier by a local axis in the testis: role of laminin alpha2 in the basement
960 membrane." FASEB J **31**(2): 584-597.
961 Ghosh, S. and P. W. Sternberg (2014). "Spatial and molecular cues for cell outgrowth during C.
962 elegans uterine development." Dev Biol **396**(1): 121-135.
963 Gianakas, C. A., D. P. Keeley, W. Ramos-Lewis, K. Park, R. Jayadev, I. W. Kenny, Q. Chi and D.
964 R. Sherwood (2023). "Hemicentin-mediated type IV collagen assembly strengthens juxtaposed
965 basement membrane linkage." J Cell Biol **222**(1).
966 Gieseler, K., H. Qadota and G. M. Benian (2017). "Development, structure, and maintenance of
967 C. elegans body wall muscle." WormBook **2017**: 1-59.
968 Goh, L. K. and A. Sorkin (2013). "Endocytosis of receptor tyrosine kinases." Cold Spring Harb
969 Perspect Biol **5**(5): a017459.
970 Gross, O., B. Beirowski, S. J. Harvey, C. McFadden, D. Chen, S. Tam, P. S. Thorner, N. Smyth, K.
971 Addicks, W. Bloch, Y. Ninomiya, Y. Sado, M. Weber and W. F. Vogel (2004). "DDR1-deficient

mice show localized subepithelial GBM thickening with focal loss of slit diaphragms and proteinuria." Kidney Int **66**(1): 102-111.
Hagedorn, E. J., H. Yashiro, J. W. Ziel, S. Ihara, Z. Wang and D. R. Sherwood (2009). "Integrin acts upstream of netrin signaling to regulate formation of the anchor cell's invasive membrane in C. elegans." Dev Cell **17**(2): 187-198.
Hisamoto, N., Y. Nagamori, T. Shimizu, S. I. Pastuhov and K. Matsumoto (2016). "The C. elegans Discoidin Domain Receptor DDR-2 Modulates the Met-like RTK-JNK Signaling Pathway in Axon Regeneration." PLoS Genet **12**(12): e1006475.
Hohenester, E. and P. D. Yurchenco (2013). "Laminins in basement membrane assembly." Cell Adh Migr **7**(1): 56-63.
Jayadev, R., Q. Chi, D. P. Keeley, E. L. Hastie, L. C. Kelley and D. R. Sherwood (2019). "alpha-Integrins dictate distinct modes of type IV collagen recruitment to basement membranes." J Cell Biol **218**(9): 3098-3116.
Jayadev, R., M. Morais, J. M. Ellingford, S. Srinivasan, R. W. Naylor, C. Lawless, A. S. Li, J. F. Ingham, E. Hastie, Q. Chi, M. Fresquet, N. M. Koudis, H. B. Thomas, R. T. O'Keefe, E. Williams, A. Adamson, H. M. Stuart, S. Banka, D. Smedley, C. Genomics England Research, D. R. Sherwood and R. Lennon (2022). "A basement membrane discovery pipeline uncovers network complexity, regulators, and human disease associations." Sci Adv **8**(20): eabn2265.
Jayadev, R. and D. R. Sherwood (2017). "Basement membranes." Curr Biol **27**(6): R207-R211.
Juskaite, V., D. S. Corcoran and B. Leitinger (2017). "Collagen induces activation of DDR1 through lateral dimer association and phosphorylation between dimers." Elife **6**.
Kamath, R. S. and J. Ahringer (2003). "Genome-wide RNAi screening in Caenorhabditis elegans." Methods **30**(4): 313-321.
Keeley, D. P., E. Hastie, R. Jayadev, L. C. Kelley, Q. Chi, S. G. Payne, J. L. Jeger, B. D. Hoffman and D. R. Sherwood (2020). "Comprehensive Endogenous Tagging of Basement Membrane Components Reveals Dynamic Movement within the Matrix Scaffolding." Dev Cell **54**(1): 60-74 e67.
Keeley, D. P. and D. R. Sherwood (2019). "Tissue linkage through adjoining basement membranes: The long and the short term of it." Matrix Biol **75-76**: 58-71.
Kelley, L. C., Q. Chi, R. Caceres, E. Hastie, A. J. Schindler, Y. Jiang, D. Q. Matus, J. Plastino and D. R. Sherwood (2019). "Adaptive F-Actin Polymerization and Localized ATP Production Drive Basement Membrane Invasion in the Absence of MMPs." Dev Cell **48**(3): 313-328 e318.
Kelley, L. C., Z. Wang, E. J. Hagedorn, L. Wang, W. Shen, S. Lei, S. A. Johnson and D. R. Sherwood (2017). "Live-cell confocal microscopy and quantitative 4D image analysis of anchor-cell invasion through the basement membrane in Caenorhabditis elegans." Nat Protoc **12**(10): 2081-2096.
Khoshnoodi, J., V. Pedchenko and B. G. Hudson (2008). "Mammalian collagen IV." Microsc Res Tech **71**(5): 357-370.
Lee, M., E. J. Cram, B. Shen and J. E. Schwarzbauer (2001). "Roles for beta(pat-3) integrins in development and function of Caenorhabditis elegans muscles and gonads." J Biol Chem **276**(39): 36404-36410.
Leitinger, B. (2014). "Discoidin domain receptor functions in physiological and pathological conditions." Int Rev Cell Mol Biol **310**: 39-87.

1015 Lilja, J., T. Zacharchenko, M. Georgiadou, G. Jacquemet, N. De Franceschi, E. Peuhu, H. Hamidi,
1016 J. Pouwels, V. Martens, F. H. Nia, M. Beifuss, T. Boeckers, H. J. Kreienkamp, I. L. Barsukov and
1017 J. Ivaska (2017). "SHANK proteins limit integrin activation by directly interacting with Rap1
1018 and R-Ras." Nat Cell Biol **19**(4): 292-305.
1019 Martin-Bermudo, M. D. and N. H. Brown (1999). "Uncoupling integrin adhesion and signaling:
1020 the betaPS cytoplasmic domain is sufficient to regulate gene expression in the Drosophila
1021 embryo." Genes Dev **13**(6): 729-739.
1022 Merchant, S. N., B. J. Burgess, J. C. Adams, C. E. Kashtan, M. C. Gregory, P. A. Santi, R. Colvin,
1023 B. Collins and J. B. Nadol, Jr. (2004). "Temporal bone histopathology in alport syndrome."
1024 Laryngoscope **114**(9): 1609-1618.
1025 Mihai, C., M. Chotani, T. S. Elton and G. Agarwal (2009). "Mapping of DDR1 distribution and
1026 oligomerization on the cell surface by FRET microscopy." J Mol Biol **385**(2): 432-445.
1027 Moerman, D. G. and B. D. Williams (2006). "Sarcomere assembly in C. elegans muscle."
1028 WormBook: 1-16.
1029 Mok, D. Z., P. W. Sternberg and T. Inoue (2015). "Morphologically defined sub-stages of C.
1030 elegans vulval development in the fourth larval stage." BMC Dev Biol **15**: 26.
1031 Morrissey, M. A., D. P. Keeley, E. J. Hagedorn, S. T. H. McClatchey, Q. Chi, D. H. Hall and D. R.
1032 Sherwood (2014). "B-LINK: a hemicentin, plakin, and integrin-dependent adhesion system that
1033 links tissues by connecting adjacent basement membranes." Dev Cell **31**(3): 319-331.
1034 Morrissey, M. A. and D. R. Sherwood (2015). "An active role for basement membrane assembly
1035 and modification in tissue sculpting." J Cell Sci **128**(9): 1661-1668.
1036 Murphy, J. E., B. E. Padilla, B. Hasdemir, G. S. Cottrell and N. W. Bunnett (2009). "Endosomes: a
1037 legitimate platform for the signaling train." Proc Natl Acad Sci U S A **106**(42): 17615-17622.
1038 Naylor, R. W., M. Morais and R. Lennon (2021). "Complexities of the glomerular basement
1039 membrane." Nat Rev Nephrol **17**(2): 112-127.
1040 Newman, A. P., J. G. White and P. W. Sternberg (1996). "Morphogenesis of the C. elegans
1041 hermaphrodite uterus." Development **122**(11): 3617-3626.
1042 Pani, A. M. and B. Goldstein (2018). "Direct visualization of a native Wnt in vivo reveals that a
1043 long-range Wnt gradient forms by extracellular dispersal." Elife **7**.
1044 Park, J. O., J. Pan, F. Mohrlen, M. O. Schupp, R. Johnsen, D. L. Baillie, R. Zapf, D. G. Moerman
1045 and H. Hutter (2010). "Characterization of the astacin family of metalloproteases in C. elegans."
1046 BMC Dev Biol **10**: 14.
1047 Payne, L. S. and P. H. Huang (2014). "Discoidin domain receptor 2 signaling networks and
1048 therapy in lung cancer." J Thorac Oncol **9**(6): 900-904.
1049 Pozzi, A., P. D. Yurchenco and R. V. Iozzo (2017). "The nature and biology of basement
1050 membranes." Matrix Biol **57-58**: 1-11.
1051 Rual, J. F., J. Ceron, J. Koreth, T. Hao, A. S. Nicot, T. Hirozane-Kishikawa, J. Vandenhaute, S. H.
1052 Orkin, D. E. Hill, S. van den Heuvel and M. Vidal (2004). "Toward improving Caenorhabditis
1053 elegans phenome mapping with an ORFeome-based RNAi library." Genome Res **14**(10B): 2162-
1054 2168.
1055 Sandri, C., F. Caccavari, D. Valdembri, C. Camillo, S. Veltel, M. Santambrogio, L. Lanzetti, F.
1056 Bussolino, J. Ivaska and G. Serini (2012). "The R-Ras/RIN2/Rab5 complex controls endothelial

1057 cell adhesion and morphogenesis via active integrin endocytosis and Rac signaling." Cell Res
1058 **22**(10): 1479-1501.
1059 Sato, K., A. Norris, M. Sato and B. D. Grant (2014). "C. elegans as a model for membrane traffic."
1060 WormBook: 1-47.
1061 Schindelin, J., I. Arganda-Carreras, E. Frise, V. Kaynig, M. Longair, T. Pietzsch, S. Preibisch, C.
1062 Rueden, S. Saalfeld, B. Schmid, J. Y. Tinevez, D. J. White, V. Hartenstein, K. Eliceiri, P.
1063 Tomancak and A. Cardona (2012). "Fiji: an open-source platform for biological-image analysis."
1064 Nat Methods **9**(7): 676-682.
1065 Sherwood, D. R. and P. W. Sternberg (2003). "Anchor cell invasion into the vulval epithelium in
1066 C. elegans." Dev Cell **5**(1): 21-31.
1067 Singh, N. and M. Han (1995). "sur-2, a novel gene, functions late in the let-60 ras-mediated
1068 signaling pathway during Caenorhabditis elegans vulval induction." Genes Dev **9**(18): 2251-
1069 2265.
1070 Sixt, M., B. Engelhardt, F. Pausch, R. Hallmann, O. Wendler and L. M. Sorokin (2001).
1071 "Endothelial cell laminin isoforms, laminins 8 and 10, play decisive roles in T cell recruitment
1072 across the blood-brain barrier in experimental autoimmune encephalomyelitis." J Cell Biol
1073 **153**(5): 933-946.
1074 Staudinger, L. A., S. J. Spano, W. Lee, N. Coelho, D. Rajshankar, M. P. Bendeck, T. Moriarty and
1075 C. A. McCulloch (2013). "Interactions between the discoidin domain receptor 1 and beta1
1076 integrin regulate attachment to collagen." Biol Open **2**(11): 1148-1159.
1077 Stiernagle, T. (2006). "Maintenance of C. elegans." WormBook: 1-11.
1078 Suleiman, H., L. Zhang, R. Roth, J. E. Heuser, J. H. Miner, A. S. Shaw and A. Dani (2013).
1079 "Nanoscale protein architecture of the kidney glomerular basement membrane." Elife **2**: e01149.
1080 Taylor, J., T. Unsoeld and H. Hutter (2018). "The transmembrane collagen COL-99 guides
1081 longitudinally extending axons in C. elegans." Mol Cell Neurosci **89**: 9-19.
1082 Timmons, L., D. L. Court and A. Fire (2001). "Ingestion of bacterially expressed dsRNAs can
1083 produce specific and potent genetic interference in Caenorhabditis elegans." Gene **263**(1-2): 103-
1084 112.
1085 Timpl, R., H. Wiedemann, V. van Delden, H. Furthmayr and K. Kuhn (1981). "A network model
1086 for the organization of type IV collagen molecules in basement membranes." Eur J Biochem
1087 **120**(2): 203-211.
1088 Tu, H., P. Huhtala, H. M. Lee, J. C. Adams and T. Pihlajaniemi (2015). "Membrane-associated
1089 collagens with interrupted triple-helices (MACITs): evolution from a bilaterian common
1090 ancestor and functional conservation in C. elegans." BMC Evol Biol **15**: 281.
1091 Unsoeld, T., J. O. Park and H. Hutter (2013). "Discoidin domain receptors guide axons along
1092 longitudinal tracts in C. elegans." Dev Biol **374**(1): 142-152.
1093 Villasenor, R., Y. Kalaidzidis and M. Zerial (2016). "Signal processing by the endosomal system."
1094 Curr Opin Cell Biol **39**: 53-60.
1095 Vogel, B. E. and E. M. Hedgecock (2001). "Hemicentin, a conserved extracellular member of the
1096 immunoglobulin superfamily, organizes epithelial and other cell attachments into oriented line-
1097 shaped junctions." Development **128**(6): 883-894.
1098 Vogel, W. F., R. Abdulhussein and C. E. Ford (2006). "Sensing extracellular matrix: an update on
1099 discoidin domain receptor function." Cell Signal **18**(8): 1108-1116.

1100 Walser, M., C. A. Umbricht, E. Frohli, P. Nanni and A. Hajnal (2017). "beta-Integrin de-
1101 phosphorylation by the Density-Enhanced Phosphatase DEP-1 attenuates EGFR signaling in C.
1102 elegans." PLoS Genet **13**(1): e1006592.
1103 Welcker, D., C. Stein, N. M. Feitosa, J. Armistead, J. L. Zhang, S. Lutke, A. Kleinridders, J. C.
1104 Bruning, S. A. Eming, G. Sengle, A. Niehoff, W. Bloch and M. Hammerschmidt (2021).
1105 "Hemicentin-1 is an essential extracellular matrix component of the dermal-epidermal and
1106 myotendinous junctions." Sci Rep **11**(1): 17926.
1107 Wildwater, M., N. Sander, G. de Vreede and S. van den Heuvel (2011). "Cell shape and Wnt
1108 signaling redundantly control the division axis of C. elegans epithelial stem cells." Development
1109 **138**(20): 4375-4385.
1110 Xiao, Q., Y. Jiang, Q. Liu, J. Yue, C. Liu, X. Zhao, Y. Qiao, H. Ji, J. Chen and G. Ge (2015). "Minor
1111 Type IV Collagen alpha5 Chain Promotes Cancer Progression through Discoidin Domain
1112 Receptor-1." PLoS Genet **11**(5): e1005249.
1113 Xu, H., D. Bihan, F. Chang, P. H. Huang, R. W. Farndale and B. Leitinger (2012). "Discoidin
1114 domain receptors promote alpha1beta1- and alpha2beta1-integrin mediated cell adhesion to
1115 collagen by enhancing integrin activation." PLoS One **7**(12): e52209.
1116 Yochem, J. and R. K. Herman (2003). "Investigating C. elegans development through mosaic
1117 analysis." Development **130**(20): 4761-4768.
1118 Zhang, Z., K. Vuori, H. Wang, J. C. Reed and E. Ruoslahti (1996). "Integrin activation by R-ras."
1119 Cell **85**(1): 61-69.
1120

Figure 1

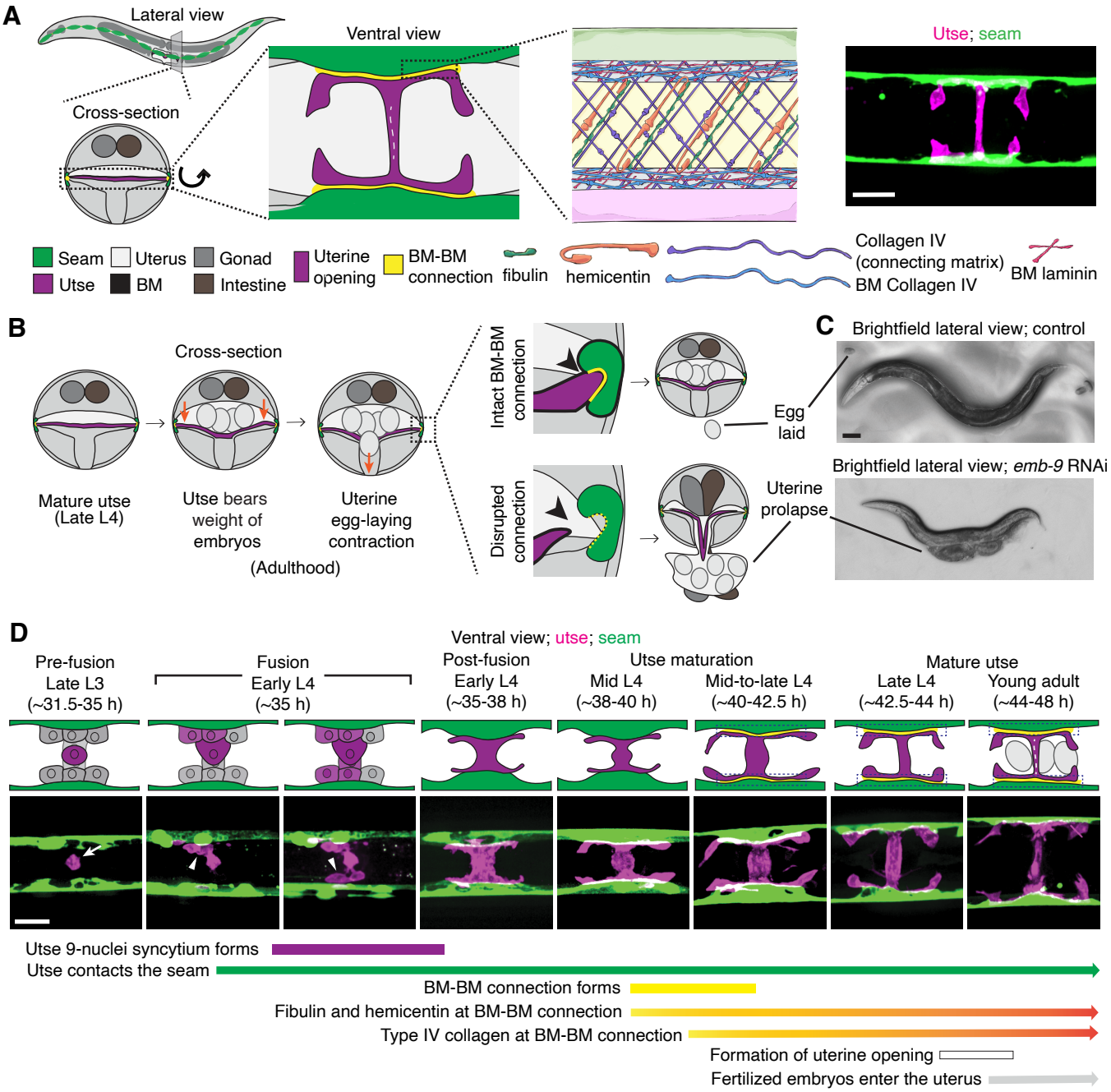

Morphogenesis of the *C. elegans* utse-seam basement membrane-basement membrane tissue connection.
(**A**) Left and center: Schematic depicting the utse-seam connection. The utse (a syncytial uterine cell) and the seam epidermal cells are both encased in basement membranes (BMs), which are linked by a BM-BM connecting matrix. Right: ventral fluorescence z-projection showing the utse and seam cells visualized by the markers *cdh-3p::mCherry::PLC* $^{\delta PH}$ and *scmp::GFP::CAAX*, respectively. (**B**) Schematic illustrating the role of the utse-seam connection in supporting the uterus during egg-laying muscle contractions. Disruption of the connection results in uterine prolapse. (**C**) Lateral brightfield images of adult worms on control RNAi treatment or RNAi against a key component of the BM-BM linkage, α1 type IV collagen/*emb-9* (RNAi fed from the L1 onward); note the uterine prolapse after loss of collagen. (**D**) A schematic summarizing the development of the utse-seam connection. Fluorescence images shown are ventral z-projections of the utse and the seam at the respective developmental stages from the late L3 to young adult (hours post-hatch at 20°C). Arrow indicates the uterine anchor cell (AC) that fuses with adjacent uterine cells to form the utse. During syncytium formation, the utse makes contact with the seam cells (arrowheads). Dotted boxes denote the BM-BM connection. Scale bars, 20 μm.

Figure 2 with 1 supplement

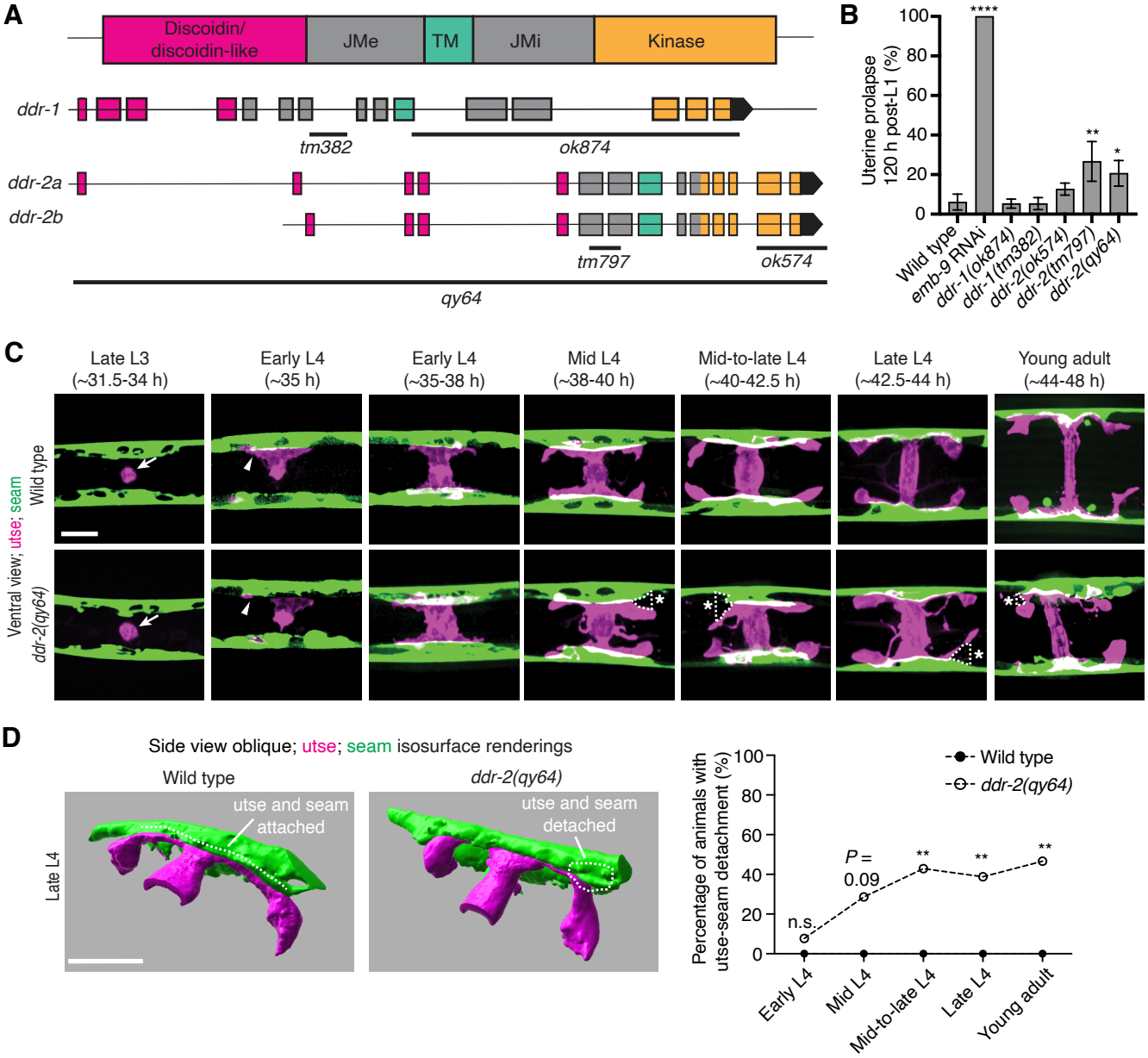

DDR-2 promotes utse-seam attachment and protects against uterine prolapse.
(**A**) Domain structure of *C. elegans* discoidin domain receptors (DDRs) and exon-intron gene structures of *ddr-1* and *ddr-2*. Exons are color coded according to respective domains. Gene regions that are deleted in respective mutant alleles (italicized text) are demarcated by solid black lines. (**B**) Frequency of uterine prolapse in *ddr-1* and *ddr-2* mutant animals compared to wild type 120 h post-L1 plating. Data are shown as mean prolapse percentage ± SD, derived from three independent trials (n = 50 animals screened per trial). α1 type IV collagen/*emb-9* RNAi was used as a positive control. ****$P \leq 0.0001$, **$P \leq 0.01$, *$P \leq 0.05$; one-way ANOVA with post hoc Dunnett's test. (**C**) Ventral fluorescence z-projections of the utse *(cdh-3p::mCherry::PLC* $^{\delta PH}$*)* and seam *(scmp::GFP::CAAX)* cells in wild-type and *ddr-2* knockout *(ddr-2(qy64))* animals from the late L3 to young adult developmental stages (hours post-hatch at 20°C). Arrows indicate the AC prior to utse formation and arrowheads denote early contacts between the utse and seam. Dotted lines with asterisks indicate regions of utse-seam detachment in *ddr-2(qy64)* animals. (**D**) Left: 3D isosurface renderings of the utse and seam in representative late L4 wild-type and *ddr-2(qy64)* animals (see also ***Figure 2—video 1***). Right: Quantification of the percentage of animals with utse-seam detachment. Wild type, early L4 to young adult: n = 0/13, n = 0/14, n = 0/22, n = 0/21, n = 0/18 animals with detachments respectively; *ddr-2(qy64)*, early L4 to young adult: n = 1/13, n = 4/14, n = 9/22, n = 7/18, n = 7/15 animals with detachments respectively. **$P \leq 0.01$, n.s. (not significant), $P > 0.05$; Fisher's exact test. Scale bars, 20 μm.

Source data 1. Source data for ***Figure 2***. Raw data of uterine prolapse frequency used to generate ***Figure 2B*** in Microsoft Excel format.

Figure 2—video 1. Animation of 3D isosurface rendering of the utse and seam in a representative late L4 wild-type animal; related to ***Figure 2D***.

Figure 3 with 1 supplement

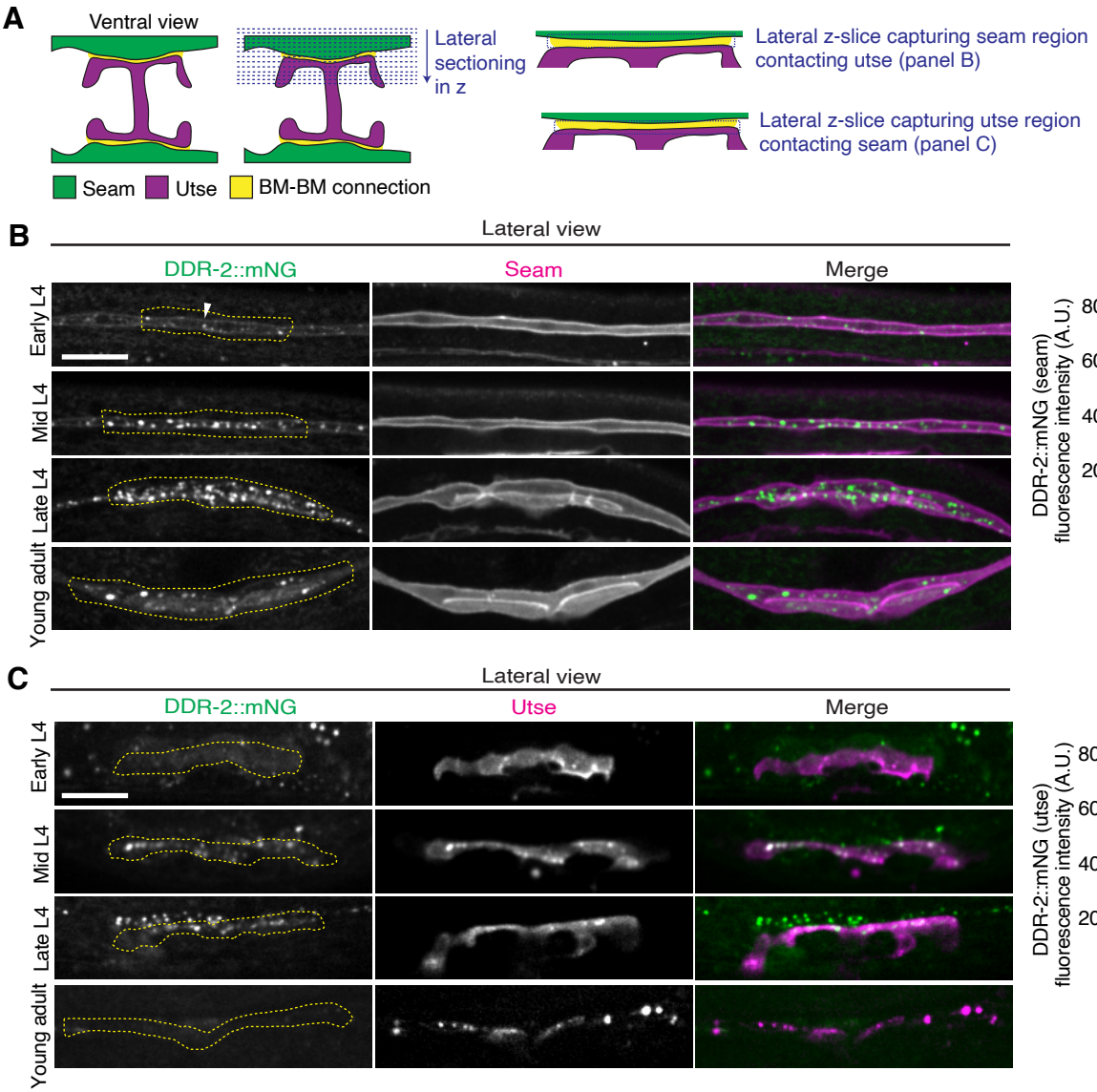

DDR-2 levels peak in the utse and seam during the formation of the BM-BM connection.
(**A**) Schematic illustrating lateral z-sectioning to determine slices that capture the seam region in contact with the utse and vice-versa. (**B**) Left: Lateral fluorescence images of DDR-2::mNG visualized with the seam marker *scmp::2xmKate2::PLC* $^{\delta PH}$ from the early L4 to young adult stages. Dotted yellow regions indicate DDR-2 signal in the seam contacting the utse. White arrowhead denotes DDR-2 signal at the cell surface. Right: Quantification of mean DDR-2::mNG fluorescence intensity in the dotted regions (n ≥ 9 for each developmental stage). ****$P \leq 0.0001$, one-way ANOVA with post hoc Dunnett's test. (**C**) Left: Lateral fluorescence images of DDR-2::mNG visualized with the utse marker *cdh-3p::mCherry::PLC* $^{\delta PH}$ from the early L4 to young adult stages. Dotted yellow regions indicate DDR-2 signal in the utse contacting the seam. Right: Quantification of mean DDR-2::mNG fluorescence intensity in dotted yellow regions (n = 10 all stages). **$P \leq 0.01$, one-way ANOVA with post hoc Dunnett's test. Scale bars, 20 μm. Box edges in boxplots represent the 25th and 75th percentiles, the line in the box denotes the median value, and whiskers mark the minimum and maximum values.

Source data 1. Source data for ***Figure 3***. Raw data of DDR-2::mNG fluorescence intensity quantification in the seam and utse used to generate boxplots in ***Figure 3B and C*** in Microsoft Excel format. Note that the boxplot in ***Figure 3—figure supplement 1A*** was also generated from these data.
Source data 2. Source data for ***Figure 3—figure supplement 1***. Raw data of DDR-2::mNG and mCherry-tagged vesicle marker co-localization analysis used to generate boxplots in ***Figure 3—figure supplement 1B and C*** in Microsoft Excel format.

Figure supplement 1. DDR-2 is found within endocytic vesicles; related to ***Figure 3B and C***.

Figure 3—figure supplement 1

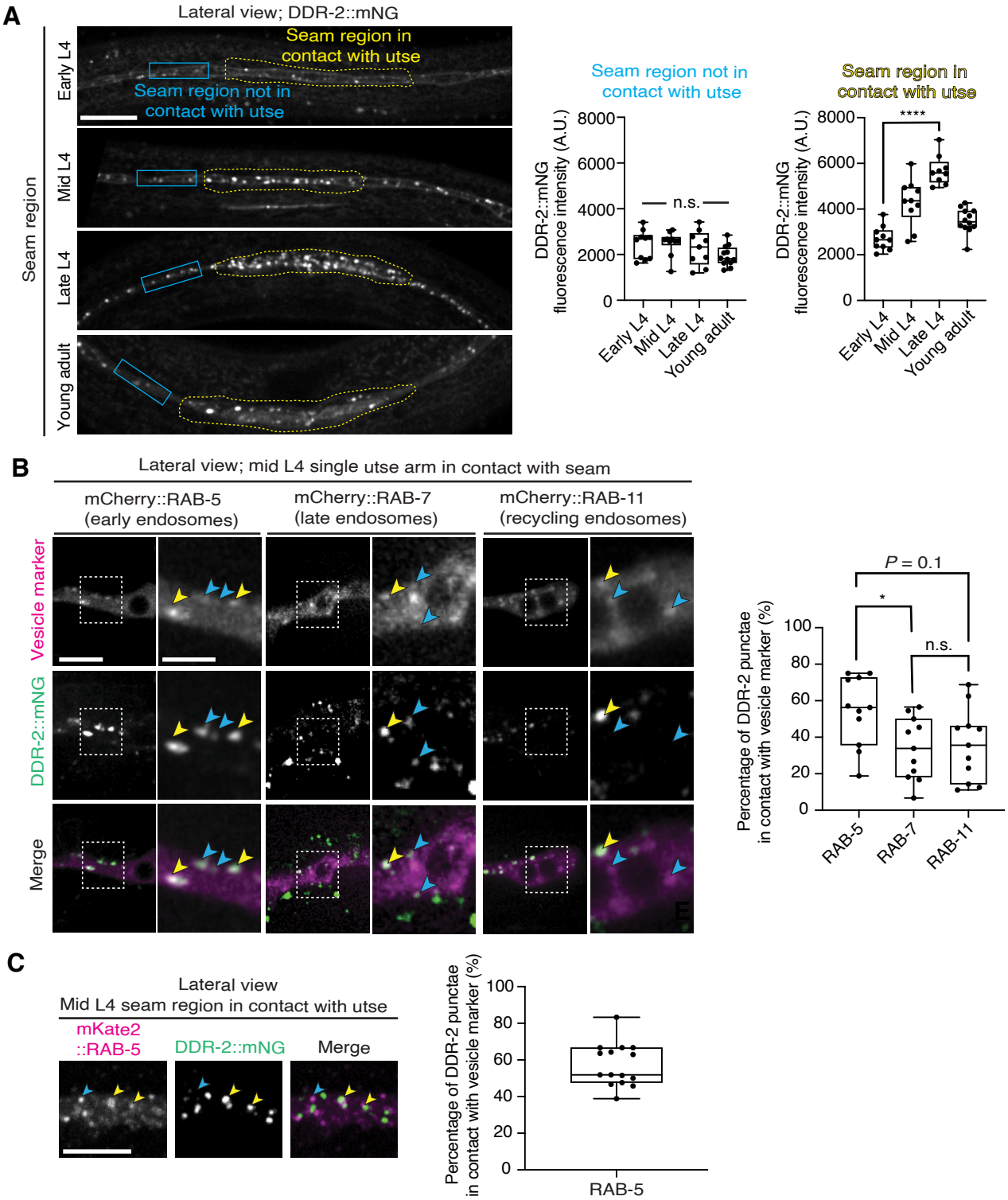

DDR-2 is found within endocytic vesicles.
Related to ***Figure 3***. (**A**) Lateral fluorescence images of DDR-2::mNG in the seam cells from the early L4 to young adult stages. Note that these images are the same animals as in ***Figure 3B*** with a larger cropped field of view to include regions of the seam not in contact with the utse. Quantification of mean fluorescence intensity in the blue and yellow boxed regions is shown on the right (n ≥ 9 all stages). Boxplots for yellow boxed regions are reproduced from ***Figure 3B***. n.s. (not significant), $P > 0.05$; Kruskal-Wallis H test. ****$P \leq 0.0001$, one-way ANOVA with post hoc Dunnett's test. (**B**) Lateral fluorescence images of DDR-2::mNG within a single arm of the utse tissue at the mid L4 stage, visualized together with mCherry-tagged RAB-5, RAB-7, or RAB-11. Boxed regions are magnified on the right. Yellow arrowheads denote DDR-2 punctae in contact with the respective vesicle marker, while blue arrowheads correspond to DDR-2 puncta that not in contact with vesicle markers. The boxplot shows quantification of percentage overlap of DDR-2 punctae with vesicle markers (n = 11 animals per marker). *$P \leq 0.05$, n.s. (not significant), $P > 0.05$; one-way ANOVA with post hoc Dunnett's T3 test. (**C**) Left: Lateral fluorescence images of DDR-2::mNG and mKate2::RAB-5 in the seam region contacting the utse. Arrowheads denote DDR-2 punctae in contact with (yellow) or not in contact with (blue) mCherry::RAB-5 punctae. Right: Percentage overlap of DDR-2 punctae with RAB-5 (n = 15). Scale bars, 20 μm. Box edges in boxplots represent the 25th and 75th percentiles, the line in the box denotes the median value, and whiskers mark the minimum and maximum values.

Figure 4 with 1 supplement

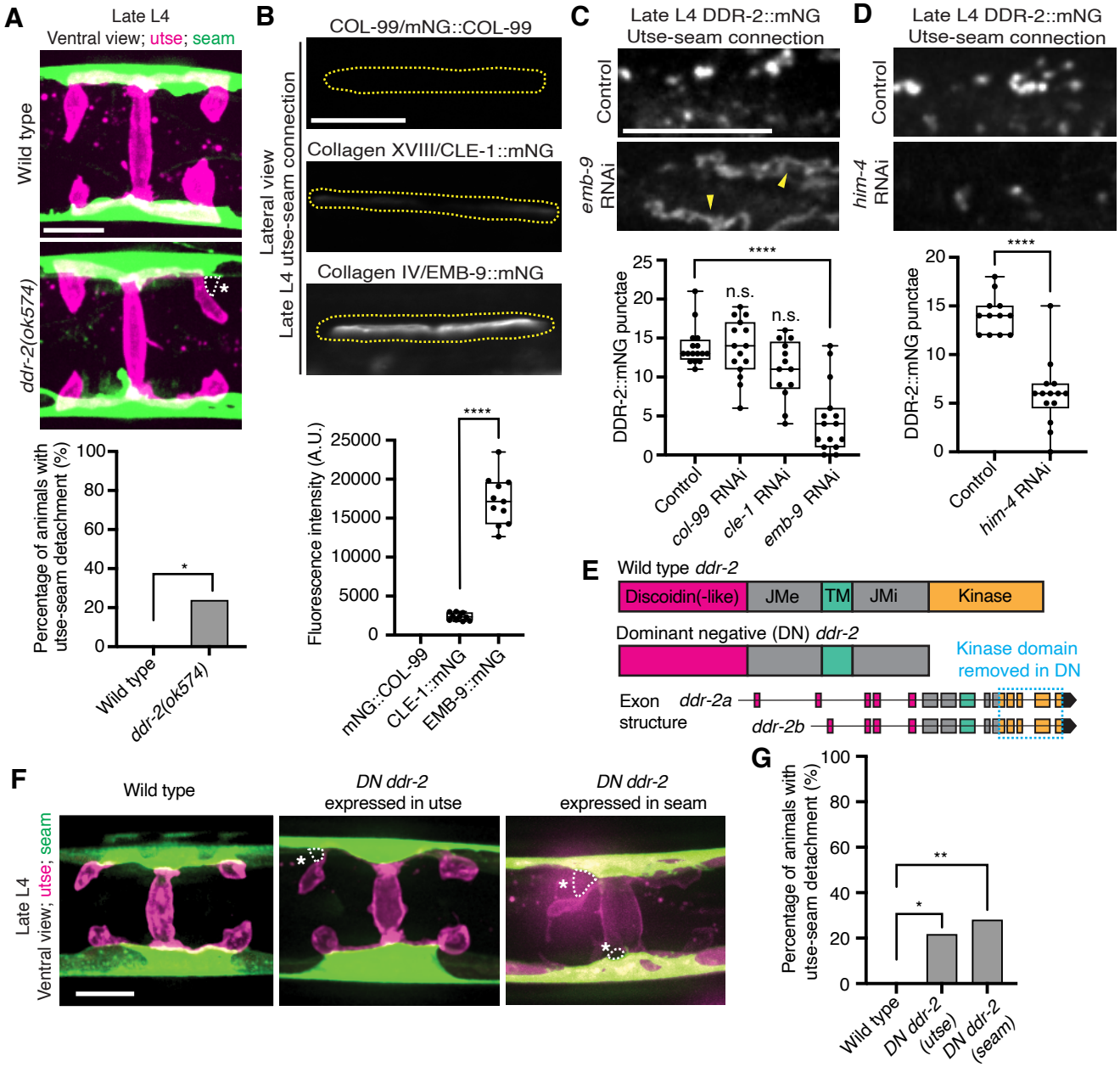

DDR-2 endocytosis is triggered by type IV collagen and DDR-2 is required in both the utse and seam to promote tissue connection.
(**A**) Top: Ventral fluorescence z-projections of the utse *(nas-22p::2xmKate2::PLC* $^{\delta PH}$*)* and seam *(scmp::GFP::CAAX)* cells in late L4 wild-type and *ddr-2* kinase domain truncation mutant *(ddr-2(ok574))* animals. Dotted lines with asterisks indicate regions of utse-seam detachment. Bottom: Quantification of the percentage of animals with utse-seam detachment. Wild type, n = 0/26; *ddr-2(ok574)*, n = 5/21 animals with detachments respectively. $^{**}P \leq 0.01$, Fisher's exact test. (**B**) Top: Lateral fluorescence images of COL-99 (mNG::COL-99), type XVIII collagen (CLE-1::mNG), and α1 type IV collagen (EMB-9::mNG) at the utse-seam connection (dotted yellow regions) of late L4 animals. All images were acquired at the same exposure. Bottom: Quantification of mean fluorescence intensity (n ≥ 10 for each fluorescent protein). $^{****}P \leq 0.0001$, unpaired two-tailed Student's *t* test. (**C**) Top: Lateral fluorescence z-projections of DDR-2::mNG at the utse-seam connection in control or *emb-9* RNAi-treated late L4 animals. Note that the field of view contains a single utse arm contacting the seam tissue. Arrowheads indicate cell surface accumulation of DDR-2 upon collagen IV depletion. Bottom: Quantification of the average number of discrete DDR-2 punctae at the utse-seam connection on control, *col-99*, *cle-1*, or *emb-9* RNAi treatments (n ≥ 13 animals for all treatments). $^{****}P \leq 0.0001$, n.s. (not significant), $P > 0.05$; Kruskal-Wallis *H* test with post hoc Dunn's test. (**D**) Top: Lateral fluorescence z-projections of DDR-2::mNG at the utse-seam attachment in control or hemicentin/*him-4* RNAi-treated late L4 animals. Bottom: Quantification of the average number of discrete DDR-2 punctae at the utse-seam attachment on control or *him-4* RNAi-treated animals (n ≥ 13 all treatments). $^{****}P \leq 0.0001$, Mann-Whitney *U* test. (**E**) Schematic of dominant negative (DN) *ddr-2*. (**F**) Ventral fluorescence z-projections of the utse *(nas-22p::2xmKate2::PLC* $^{\delta PH}$*)* and seam *(wrt-2p::GFP::PLC* $^{\delta PH}$*)* tissues in late L4 stage wild-type animals and animals expressing *DN ddr-2* in the utse (driven by *cdh-3* promoter) or the seam (driven by *scm* promoter). Dotted lines with asterisks indicate regions of utse-seam detachment. (**G**) Quantification of the percentage of animals with utse-seam detachment. Wild type, n = 0/23; *DN ddr-2(utse)*, n = 5/23; *DN ddr-2(seam)*, n = 7/25 animals with detachments respectively. $^{**}P \leq 0.01$, $^{*}P \leq 0.05$; Fisher's exact test. Scale bars, 20 μm. Box edges in boxplots represent the 25th and 75th percentiles, the line in the box denotes the median value, and whiskers mark the minimum and maximum values.

Source data 1. Source data for ***Figure 4***. Raw data of fluorescence intensity quantification of tagged collagen ligands at the utse-seam connection used to generate boxplot in ***Figure 4B***, and raw data of DDR-2::mNG puncta counts at the utse-seam connection upon collagen ligand or hemicentin depletion used to generate boxplots in ***Figure 4C and D*** in Microsoft Excel format.
Source data 2. Source data for ***Figure 4—figure supplement 1***. Raw data of quantification of knockdown efficiencies of tagged collagen ligands and hemicentin at the utse-seam connection used to generate boxplots in ***Figure 4—figure supplement 1*** in Microsoft Excel format.

Figure supplement 1. Collagen and hemicentin knockdown efficiencies; related to ***Figure 4C and D***.

Figure 4—figure supplement 1

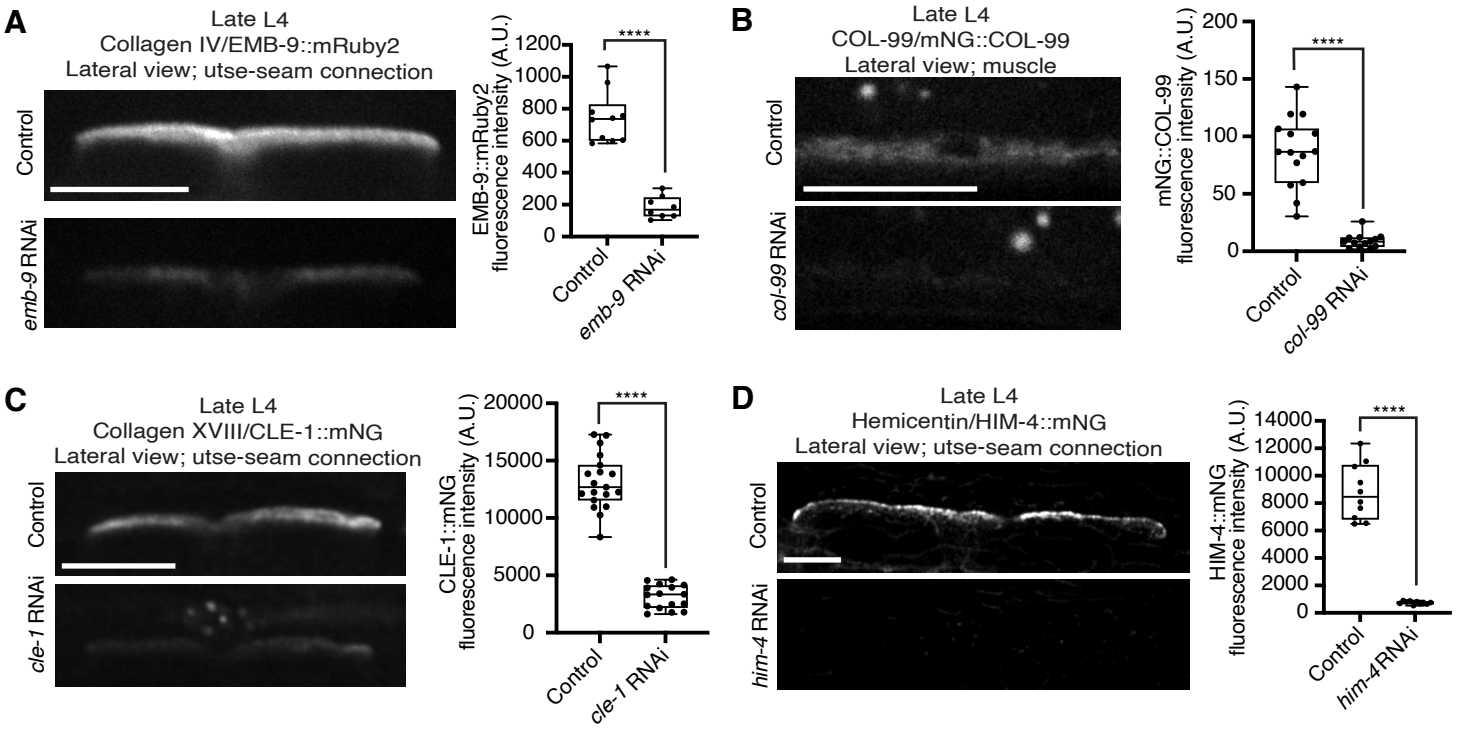

Collagen and hemicentin knockdown efficiencies.
Related to ***Figure 4***. (**A**) Lateral fluorescence images of EMB-9::mRuby2 (type IV collagen) at the utse-seam BM-BM connection in late L4 control or *emb-9* RNAi-treated animals. Mean fluorescence intensity quantified on the right (n ≥ 8 all treatments). (**B**) Lateral fluorescence images of mNG::COL-99 (COL-99) in the body wall muscle tissue in late L4 control or *col-99* RNAi-treated animals. Mean fluorescence intensity quantified on the right (n ≥ 13 all treatments). COL-99 signal in the muscle was analyzed as COL-99 was not detected at the utse-seam connection. (**C**) Lateral fluorescence images of CLE-1::mNG (type XVIII collagen) at the utse-seam BM-BM attachment in late L4 control or *cle-1* RNAi-treated animals. Mean fluorescence intensity quantified on the right (n ≥ 16 all treatments). (**D**) Lateral fluorescence images of HIM-4::mNG (hemicentin) at the utse-seam BM-BM connection in late L4 control or *him-4* RNAi-treated animals. Mean fluorescence intensity quantified on the right (n = 10 all treatments). ****$P \leq 0.0001$, unpaired two-tailed Student's *t* test (EMB-9, CLE-1, and HIM-4) or Mann-Whitney *U* test (COL-99). Scale bars, 20 μm. Box edges in boxplots represent the 25th and 75th percentiles, the line in the box denotes the median value, and whiskers mark the minimum and maximum values.

Figure 5 with 2 supplements

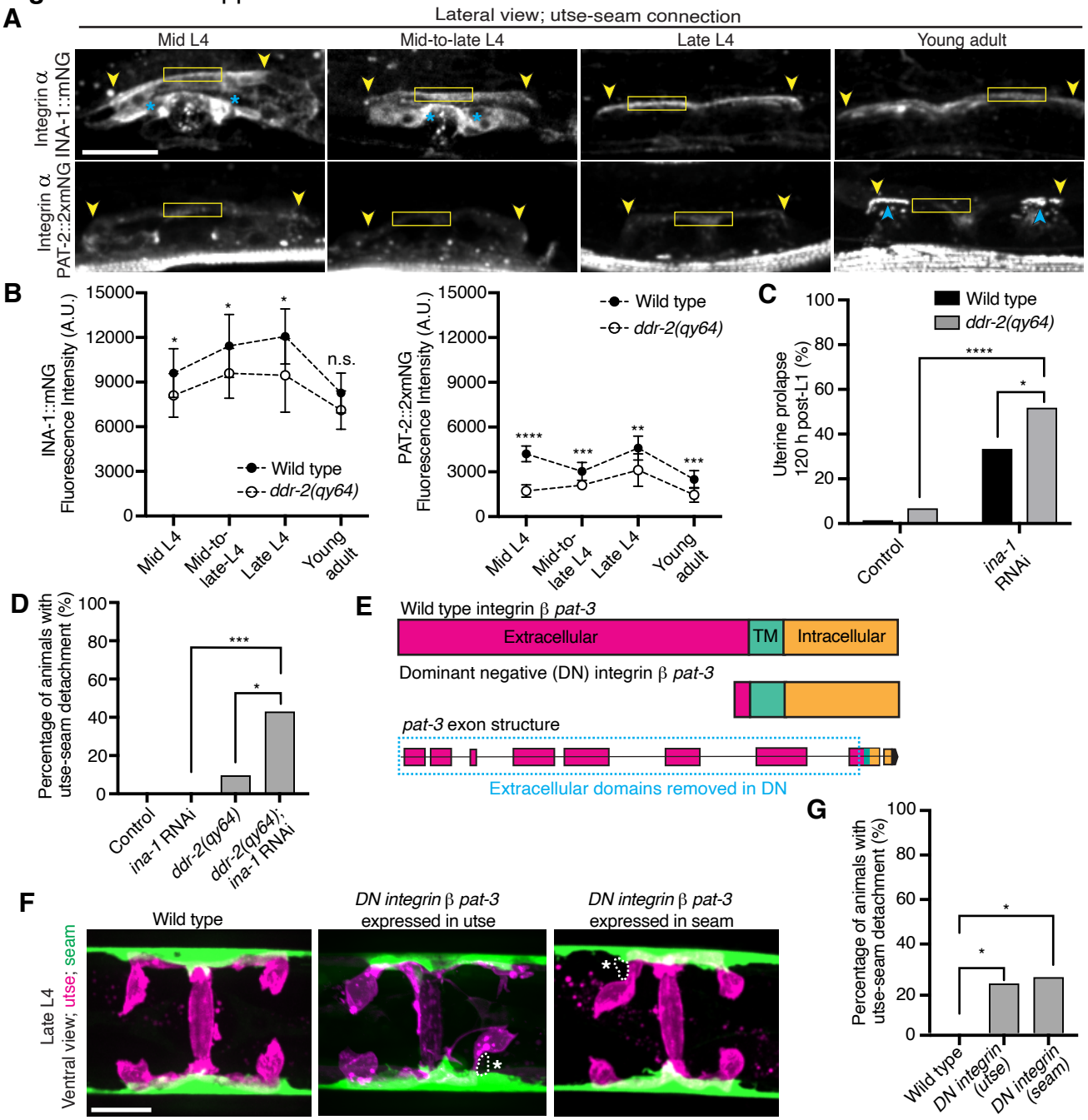

DDR-2 regulates integrin levels at the utse-seam connection and integrin functions in the utse and seam to mediate tissue attachment. (**A**) Lateral fluorescence z-projections of integrin α subunits INA-1::mNG and PAT-2::2XmNG at the utse-seam connection (yellow arrowheads) from the mid L4 to young adult stages. Blue asterisks and arrowheads denote INA-1 signal in the developing vulva and PAT-2 at muscle attachment sites respectively. Fluorescence intensity at the utse-seam connection measured in yellow boxes. (**B**) Quantification of mean fluorescence intensity in wild-type and *ddr-2* knockout *(ddr-2(qy64))* animals (n ≥ 9 all conditions). Error bars represent SD. ****$P \leq 0.0001$, ***$P \leq 0.001$, **$P \leq 0.01$, *$P \leq 0.05$, n.s. (not significant), P > 0.05; unpaired two-tailed Student's *t* test. (**C**) Frequency of uterine prolapse in wild-type and *ddr-2(qy64)* animals treated with control or *ina-1* RNAi 120 h post-L1 plating. Control n = 1/70, *ddr-2(qy64)* n = 4/60, *ina-1* RNAi n = 22/66, and *ddr-2(qy64)*; *ina-1* RNAi n = 31/60 animals with uterine prolapse respectively. ****$P \leq 0.0001$, *$P \leq 0.05$; Fisher's exact test. (**D**) Frequency of utse-seam detachments in late L4 wild-type and *ddr-2(qy64)* animals treated with control or *ina-1* RNAi. Control n = 0/21, *ina-1* RNAi n = 0/25, *ddr-2(qy64)* n = 2/21, and *ddr-2(qy64)*; *ina-1* RNAi n = 9/21 animals with detachments respectively. ***$P \leq 0.001$, *$P \leq 0.05$; Fisher's exact test. (**E**) Schematic of dominant negative (DN) β integrin *pat-3*. (**F**) Ventral fluorescence z-projections of the utse *(cdh-3p::mCherry::PLC $^{\delta PH}$* or *nas-22p::2xmKate2::PLC $^{\delta PH}$)* and seam *(wrt-2p::GFP::PLC $^{\delta PH}$* or *scmp::GFP::CAAX)* cells in late L4 wild-type animals and animals expressing *DN integrin* in the utse (*zmp-1$^{mk50-51}$* promoter) or the seam (*wrt-2* promoter). Dotted lines with asterisks indicate regions of utse-seam detachment. (**G**) Percentage of animals with utse-seam detachment. Wild type, n = 0/19; *DN integrin (utse)*, n = 4/18; *DN integrin (seam)*, n = 4/16 animals with detachments respectively. *$P \leq 0.05$, Fisher's exact test. Scale bars, 20 μm.

Source data 1. Source data for ***Figure 5***. Raw data of INA-1/PAT-2 fluorescence intensity quantification used to generate ***Figure 5B*** in Microsoft Excel format.
Source data 2. Source data for ***Figure 5—figure supplement 1***. Raw data of fluorescence intensity quantification of matrix components and ZMP-4 at the utse-seam BM-BM linkage used to generate boxplots in ***Figure 5—figure supplement 1*** in Microsoft Excel format.
Source data 3. Source data for ***Figure 5—figure supplement 2***. Raw data of fluorescence intensity quantification of *ina-1* knockdown used to generate plots in ***Figure 5—figure supplement 2D and E*** in Microsoft Excel format.

Figure supplement 1. *ddr-2* loss does not reduce functional levels of fibulin, hemicentin, type IV collagen, and matrix metalloproteinase ZMP-4 at the utse-seam connection; related to ***Figure 5***.
Figure supplement 2. The integrin α subunits INA-1 and PAT-2 are localized within both the utse and seam cells; related to ***Figure 5***.

Figure 5—figure supplement 1

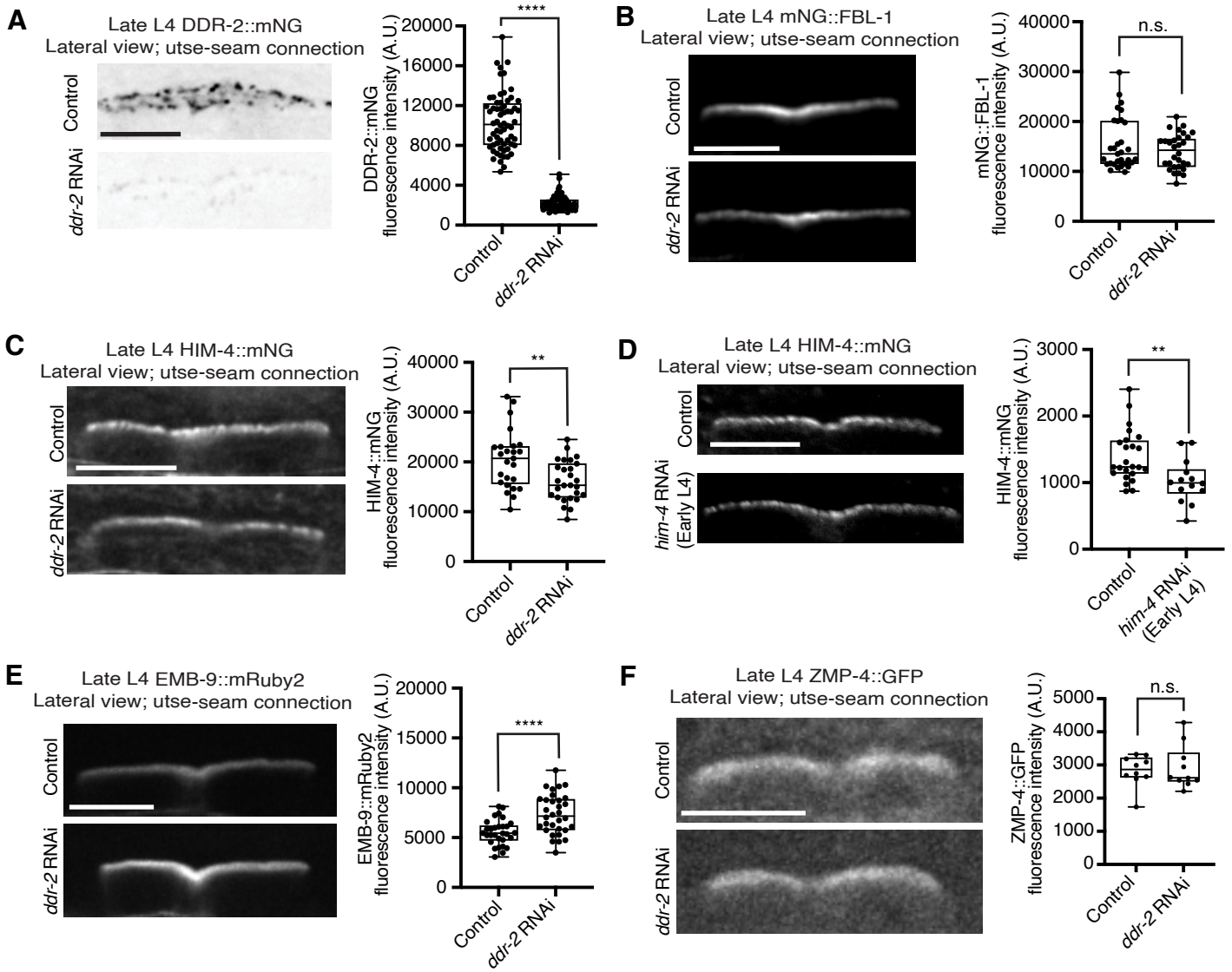

ddr-2* loss does not reduce functional levels of fibulin, hemicentin, type IV collagen, and matrix metalloproteinase ZMP-4 at the utse-seam connection.** Related to ***Figure 5. (**A**) Lateral fluorescence images of DDR-2::mNG at the utse-seam BM-BM connection in late L4 control or *ddr-2* RNAi-treated animals. Mean fluorescence intensity quantified on the right (n ≥ 60 all treatments). ****$P \leq 0.0001$, Mann-Whitney *U* test. (**B**) Lateral fluorescence images of mNG::FBL-1 (fibulin) at the utse-seam connection in late L4 control or *ddr-2* RNAi-treated animals. Mean fluorescence intensity quantified on the right (n ≥ 30 all treatments). n.s. (not significant), $P > 0.05$, Mann-Whitney *U* test. (**C**) Lateral fluorescence images of HIM-4::mNG (hemicentin) at the utse-seam tissue linkage in late L4 control or *ddr-2* RNAi-treated animals. Mean fluorescence intensity quantified on the right (n ≥ 25 all treatments). **$P \leq 0.01$, unpaired two-tailed Student's *t* test. (**D**) Lateral fluorescence images of HIM-4::mNG (hemicentin) at the utse-seam connection in late L4 control or *him-4* RNAi-treated animals. RNAi was initiated at the early L4 stage. Mean fluorescence intensity quantified on the right (n ≥ 14 all treatments). **$P \leq 0.01$, unpaired two-tailed Student's *t* test.
(**E**) Lateral fluorescence images of EMB-9::mRuby2 (type IV collagen) at the utse-seam attachment site in late L4 control or *ddr-2* RNAi-treated animals. Mean fluorescence intensity quantified on the right (n ≥ 30 all treatments). ****$P \leq 0.0001$, unpaired two-tailed Student's *t* test. (**F**) Lateral fluorescence images of matrix metalloproteinase ZMP-4::GFP at the utse-seam tissue connection in late L4 control or *ddr-2* RNAi-treated animals. Mean fluorescence intensity quantified on the right (n = 10 all treatments). n.s. (not significant), $P > 0.05$, Mann-Whitney *U* test. Scale bars, 20 μm. Box edges in boxplots represent the 25th and 75th percentiles, the line in the box denotes the median value, and whiskers mark the minimum and maximum values.

Figure 5—figure supplement 2

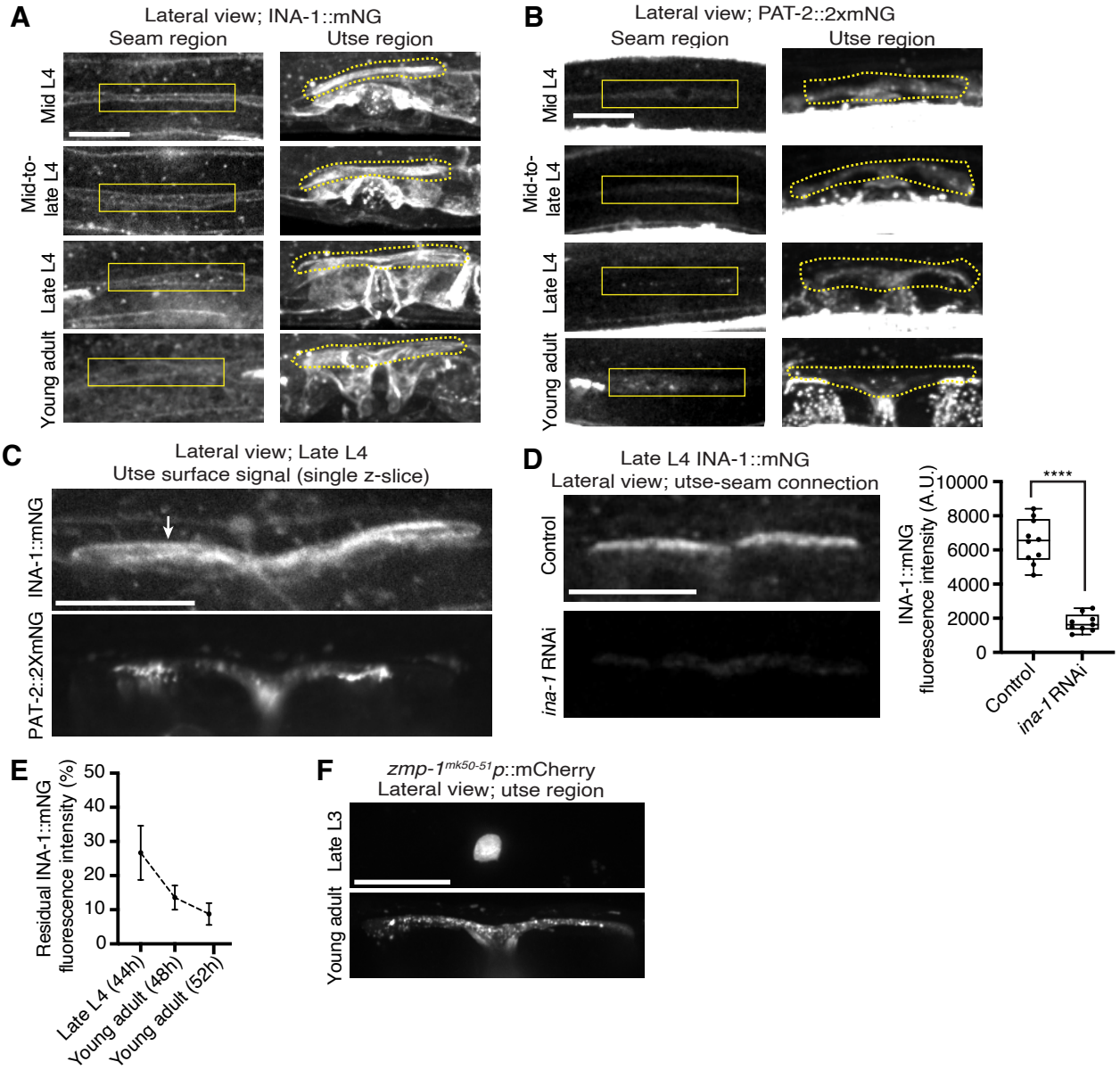

The integrin α subunits INA-1 and PAT-2 are localized within both the utse and seam cells.
Related to ***Figure 5***. (**A**) Lateral fluorescence z-projections of the integrin α subunit INA-1::mNG between the mid L4 and young adult stages. Localization in the seam and utse are indicated by solid and dotted boxed regions respectively (n ≥ 10 animals examined all stages). (**B**) Lateral fluorescence z-projections of the integrin α subunit PAT-2::2XmNG between the mid L4 and young adult stages. Localization in the seam and utse are indicated by solid and dotted boxed regions respectively (n ≥ 7 animals examined all stages). (**C**) Lateral fluorescence images of INA-1::mNG and PAT-2::2XmNG at the z-plane of the utse surface in late L4 animals (n ≥ 10 animals examined each). Arrow indicates strong INA-1 signal at the utse surface. (**D**) Lateral fluorescence images of INA-1::mNG at the utse-seam connection in late L4 control or *ina-1* RNAi-treated animals. Mean fluorescence intensity quantified on the right (n ≥ 9 all treatments). ****$P \leq 0.0001$, unpaired two-tailed Student's *t* test. (**E**) Quantification of residual INA-1::mNG fluorescence intensity at the utse-seam interface at the indicated developmental stages following *ina-1* knockdown initiated at the L1 stage. Data are represented as percentages of mean INA-1::mNG at the respective stages in control animals (n ≥ 7 animals examined all stages). Error bars denote SD. (**F**) Lateral fluorescence z-projections of mCherry driven by the *zmp-1*$^{mK50-51}$ promoter in the utse region in late L3 and young adult animals (n = 5 animals examined at each stage).

Figure 6 with 1 supplement

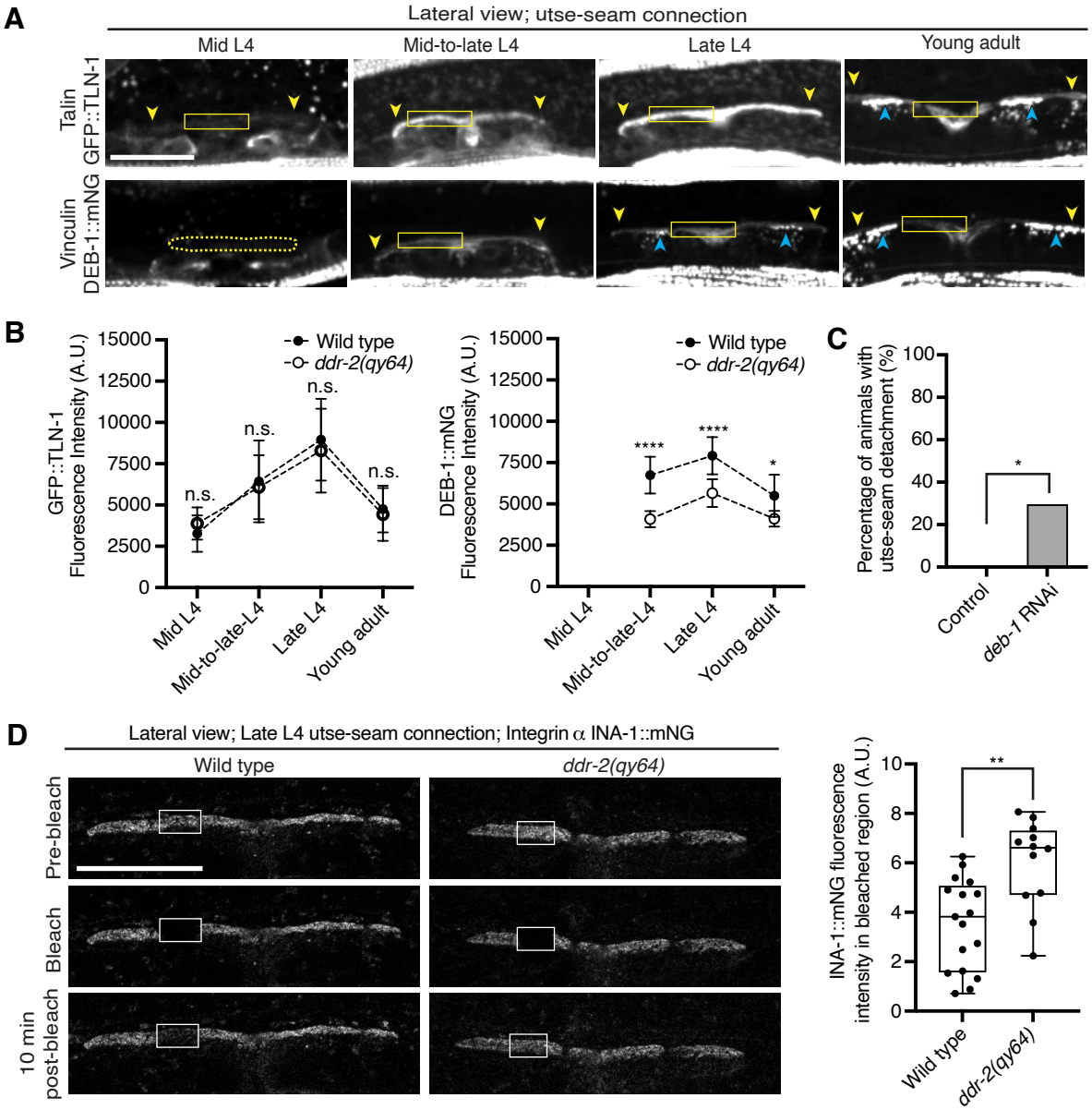

DDR-2 upregulates vinculin levels and stabilizes integrin at the utse-seam connection.
(**A**) Lateral fluorescence z-projections of the integrin activators talin (GFP::TLN-1) and vinculin (DEB-1::mNG) at the utse-seam attachment region (bounded by yellow arrowheads) from the mid L4 to young adult stages. Vinculin was not detected at the utse-seam attachment region at the mid L4 stage (dotted yellow box). Blue arrowheads indicate fluorescence signal at muscle attachment sites. Fluorescence intensity at the utse-seam attachment region was measured in the solid yellow boxes. (**B**) Quantification of TLN-1 and DEB-1 mean fluorescence intensity in wild-type and *ddr-2* knockout *(ddr-2(qy64))* animals (n ≥ 9 all conditions). Error bars represent SD. ****$P \leq 0.0001$, **$P \leq 0.01$, *$P \leq 0.05$, n.s. (not significant), $P > 0.05$; unpaired two-tailed Student's *t* test. (**C**) Frequency of utse-seam detachments observed in control or *deb-1* RNAi-treated late L4 animals. Control n = 0/21, *ina-1* RNAi n = 5/17 animals with detachments respectively. *$P \leq 0.05$, Fisher's exact test. (**D**) Left: Lateral fluorescence images of INA-1::mNG at the utse-seam connection before photobleaching, immediately after photobleaching, and 10 min post-photobleaching in late L4 wild-type and *ddr-2(qy64)* animals. Box indicates bleached region. Right: Quantification of mean INA-1::mNG fluorescence intensity in the bleached region 10 min post-photobleaching. Wild type, n = 17; *ddr-2(qy64)*, n = 12. **$P \leq 0.01$, unpaired two-tailed Student's *t* test. Scale bars, 20 μm. Box edges in boxplots represent the 25th and 75th percentiles, the line in the box denotes the median value, and whiskers mark the minimum and maximum values.

Source data 1. Source data for ***Figure 6***. Raw data of fluorescence intensity quantification of TLN-1 and DEB-1 as well as INA-1 recovery after photobleaching used to generate plots in ***Figure 6B and D*** in Microsoft Excel format.
Source data 2. Source data for ***Figure 6—figure supplement 1***. Raw data of fluorescence intensity quantification of *deb-1* knockdown at the utse-seam connection used to generate boxplot in ***Figure 6—figure supplement 1*** in Microsoft Excel format.

Figure supplement 1. *deb-1* knockdown efficiency; related to ***Figure 6C***.

Figure 6—figure supplement 1

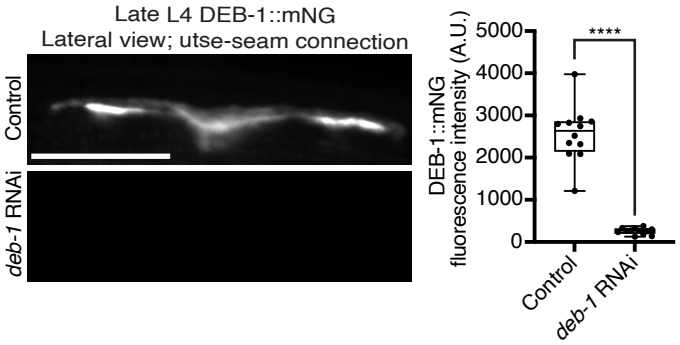

***deb-1* knockdown efficiency.**
Related to ***Figure 6***. Lateral fluorescence images of DEB-1::mNG (vinculin) at the utse-seam connection in late L4 control or *deb-1* RNAi-treated animals. Mean fluorescence intensity quantified on the right (n = 12 all treatments). ****$P \leq 0.0001$, unpaired two-tailed Student's *t* test. Scale bars, 20 μm. Box edges in boxplots represent the 25th and 75th percentiles, the line in the box denotes the median value, and whiskers mark the minimum and maximum values.

Figure 7 with 1 supplement

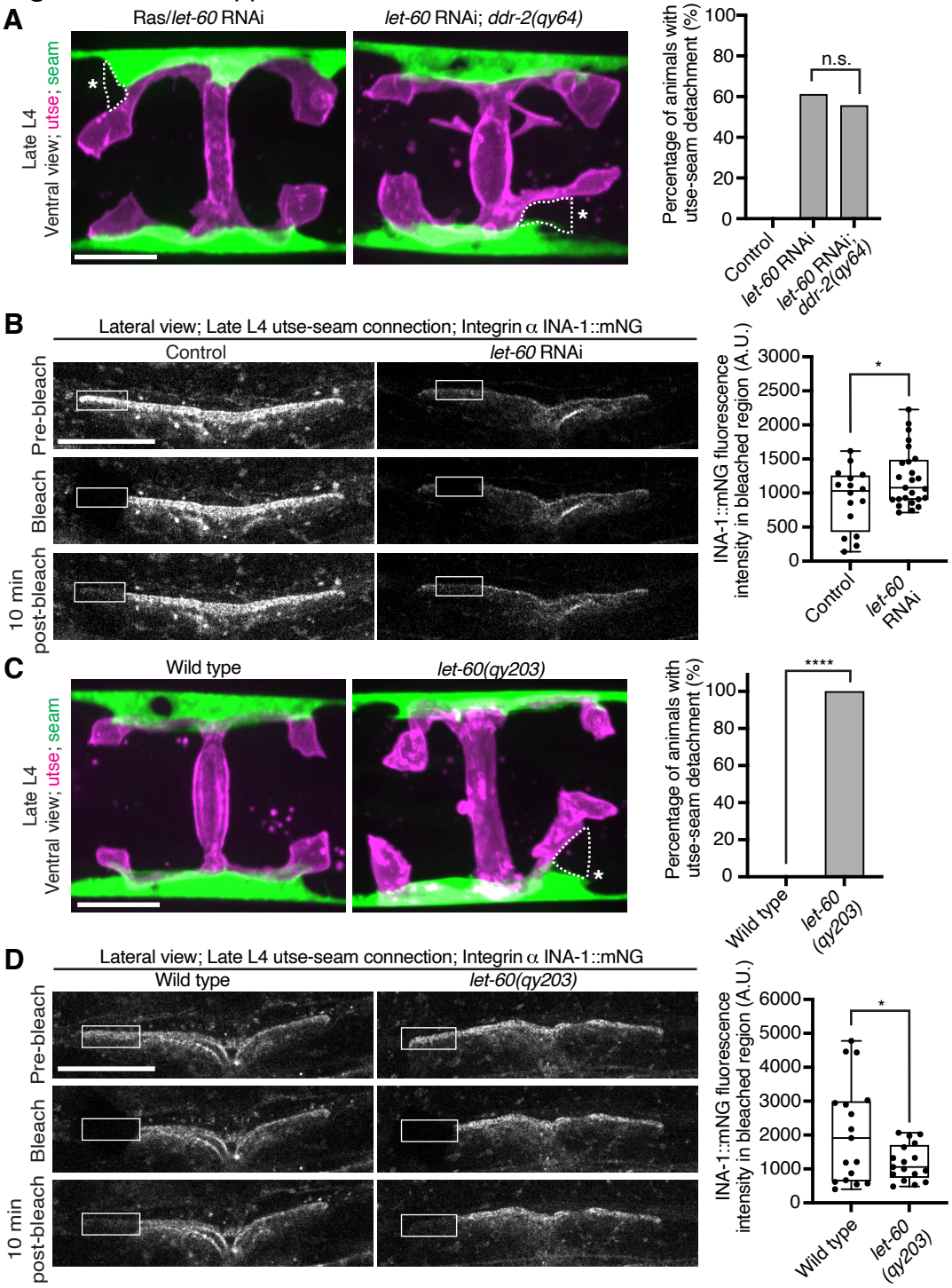

Ras/LET-60 acts in the same pathway as DDR-2 and controls integrin stability at the utse-seam tissue connection.
(**A**) Left: Ventral fluorescence z-projections of the utse *(nas-22p::2xmKate2::PLC* $^{\delta PH}$*)* and seam *(scmp::GFP::CAAX)* tissues in wild-type and *ddr-2* knockout *(ddr-2(qy64))* animals on Ras/*let-60* RNAi treatment. Dotted lines with asterisks indicate regions of utse-seam detachment. Right: Percentage of animals with utse-seam detachment. Control n = 0/21, *let-60* RNAi n = 11/18, and *let-60* RNAi; *ddr-2(qy64)*, n = 10/18 animals with detachments respectively. n.s. (not significant), $P > 0.05$; Fisher's exact test. (B) Left: Lateral fluorescence images of INA-1::mNG at the utse-seam connection before photobleaching, immediately after photobleaching, and 10 min post-photobleaching in late L4 control or *let-60* RNAi-treated animals. Box indicates bleached region. Right: Quantification of mean INA-1::mNG fluorescence intensity in the bleached region 10 min post-photobleaching. Control n = 16, *let-60* RNAi n = 25. *$P \leq 0.05$, unpaired two-tailed Student's *t* test. (C) Left: Ventral fluorescence z-projections of the utse and seam tissues in late L4 wild-type and *let-60* gain-of-function mutant *(let-60(qy203))* animals. Dotted lines with asterisks indicate regions of utse-seam detachment. Right: Quantification of utse-seam detachment frequency. Wild type, n = 0/26; *let-60(qy203)*, n = 11/11 animals with detachments respectively. ****$P \leq 0.0001$, Fisher's exact test. (D) Left: Lateral fluorescence images of INA-1::mNG at the utse-seam attachment region before photobleaching, immediately after photobleaching, and 10 min post-photobleaching in late L4 wild-type and *let-60(qy203)* animals. Box indicates bleached region. Right: Quantification of mean INA-1::mNG fluorescence intensity in the bleached region 10 min post-photobleaching (n = 17 each genotype). *$P \leq 0.05$, unpaired two-tailed Student's *t* test. Scale bars, 20 μm. Box edges in boxplots represent the 25th and 75th percentiles, the line in the box denotes the median value, and whiskers mark the minimum and maximum values.

Source data 1. Source data for ***Figure 7***. Raw data of fluorescence intensity quantification of INA-1::mNG for photobleaching experiments used to generate boxplots in ***Figure 7B and D*** in Microsoft Excel format. Note that source data for ***Figure 7—figure supplement 1*** is found within ***Source data 1***.

Figure supplement 1. Ras/*let-60* knockdown reduces INA-1::mNG levels at the utse-seam connection; related to ***Figure 7B***.

Figure 7—figure supplement 1

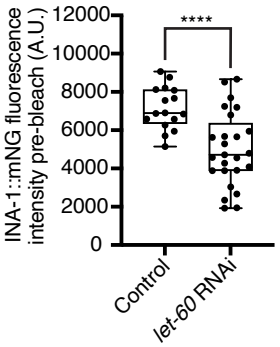

Ras/*let-60* knockdown reduces INA-1::mNG levels at the utse-seam connection.
Related to ***Figure 7***. Quantification of mean INA-1::mNG fluorescence intensity at the utse-seam connection prior to photobleaching in control or Ras/*let-60* RNAi-treated late L4 animals (see representative images in ***Figure 7B***, pre-bleach panel. Control n = 16; *let-60* RNAi n = 25. ****$P \leq 0.0001$, unpaired two-tailed Student's *t* test. Scale bars, 20 μm. Box edges in boxplots represent the 25th and 75th percentiles, the line in the box denotes the median value, and whiskers mark the minimum and maximum values.

Figure 8

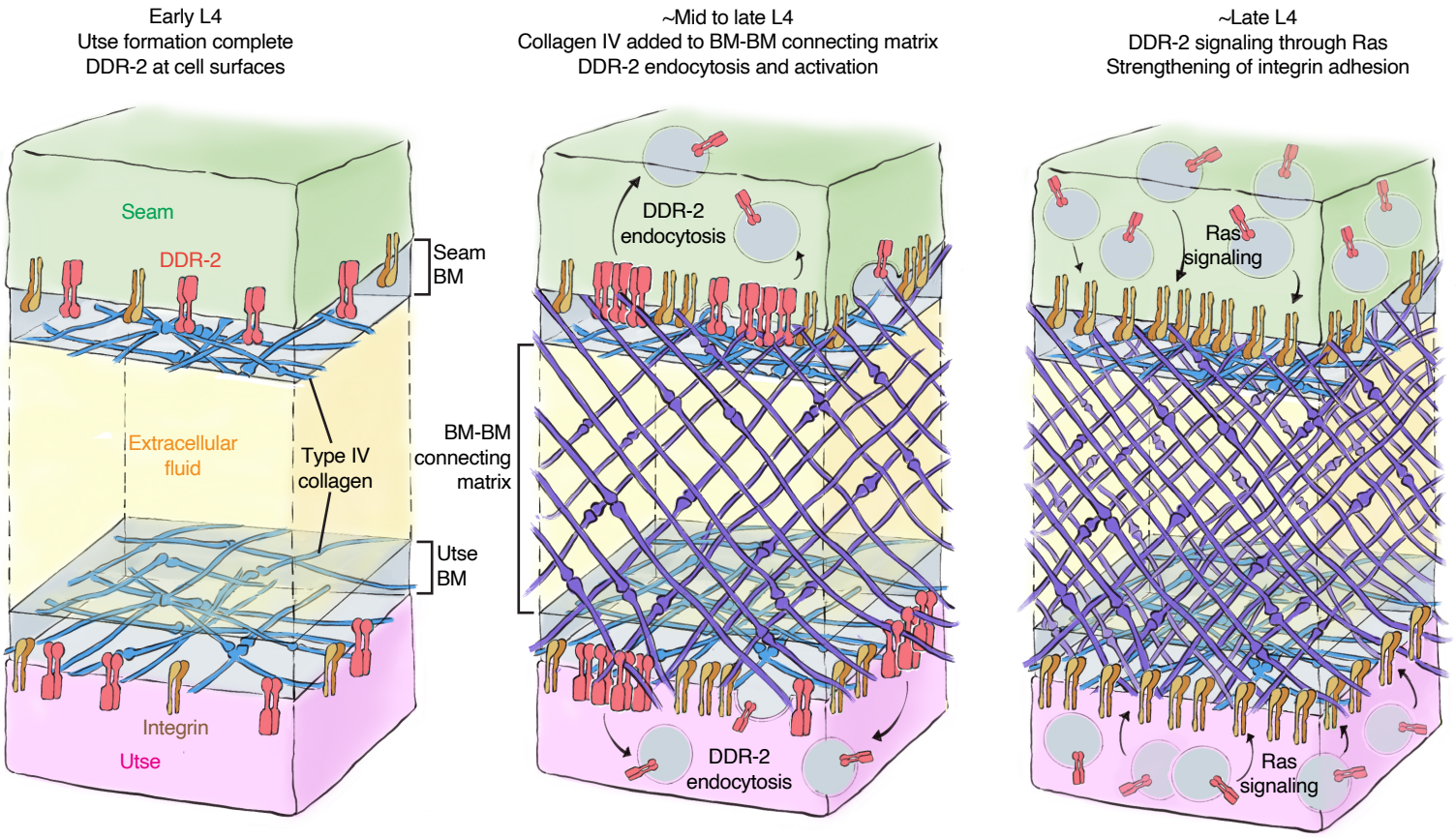

Model of DDR-2 function at the utse-seam tissue connection.
(**A**) At the early L4 larval stage, DDR-2 is predominantly found at the surfaces of utse and seam cells. (**B**) Between the mid and late L4 stages, type IV collagen assembles in the BM-BM connecting matrix to link the utse and seam tissues. Collagen addition and binding to DDR-2 triggers DDR-2 endocytosis and activation. (**C**) By the late L4, endocytic localization of DDR-2 reaches peak levels. Ras/LET-60 acts in the same pathway and may function downstream of DDR-2 to stabilize integrin adhesion. Thus, type IV collagen has a dual role in fastening the tissue connection and in signaling through DDR-2 to bolster cell adhesion at the linkage site.